A homogenized model for the nonlinear analysis of masonry columns in compression*

Daniela Addessi† and Elio Sacco‡ †

† Dipartimento di Ingegneria Strutturale e Geotecnica,
Università di Roma Sapienza, Via Eudossiana 18, 00184 Roma, Italy
‡ Dipartimento di Strutture per l'Ingegneria e l'Architettura,
Università di Napoli Federico II, Via Claudio 21, 80125 Napoli, Italy

Abstract

A homogenized model based on simplified kinematic assumptions for the analysis of masonry columns subjected to axial forces is presented. A Unit Cell (UC) characterized by different arrangements of clay bricks and mortar joints is modeled and analyzed. The kinematic unknown fields are approximated by cubic interpolation functions and the compatible strain fields are accordingly derived. Stresses in bricks and mortar are evaluated on the basis of a damage constitutive law, relying on a modified Willam-Warnke yield criterion and an exponential evolution for the damage variable. The equilibrium equations are consistently deduced via the virtual displacement principle. A numerical solution procedure is proposed and described in detail, using the collocation technique to solve the nonlinear evolution problem of damage variables in masonry constituents. Numerical applications are presented to validate the proposed model. The response of UCs characterized by different geometrical textures is numerically studied and the results are compared with those obtained by well assessed nonlinear nonlocal finite element (FE) modeling approaches. Finally, a parametric investigation on the effects of constituents mechanical properties on the overall UC response is performed and a comparison with experimental evidences is illustrated.

Keywords: Brick masonry, Micromechanical analysis, Homogenization, Damage law, Strength in compression, Collocation method.

*in press in European Journal of Mechanics - A/Solids https://doi.org/10.1016/j.euromechsol.2018.04.008
†Corresponding author (elio.sacco@unina.it)

1 Introduction

Masonry is a heterogeneous material, often made of the assemblage of clay bricks joined by mortar layers, which can be characterized by very different mechanical properties, mainly in old constructions. Both the constituents show cohesive response with softening branches in the stress-strain relationship both in tension and compression. Concerning overall masonry properties, tensile strength, mainly due to decohesion and opening of the mortar-brick interface, usually shows different values in different regions of the building and can change during the construction's lifetime. Hence, this is a very uncertain parameter commonly characterized by a low, if not negligible, value. Relying on this, no-tension models have been widely adopted, where vanishing tensile strength is considered [4, 15].

Considering that old masonry constructions are commonly characterized by very low values of operating compressive stresses with respect to the ultimate strength, failure of masonry elements is mostly due to limited tensile strength of the material, which induces opening of fractures and, hence, activation of collapse mechanisms.

Nevertheless, the accurate evaluation of masonry compressive strength is relevant to prevent crushing mechanisms that can occur for thin structural elements or reinforced masonry. This parameter depends on the nontrivial interaction between mortar and bricks and can be identified on the basis of laboratory tests on small assemblage of bricks and mortar, or via the micromechanical analysis of masonry specimens [3, 9].

Therefore, the correct determination of masonry compressive strength as a function of the mechanical properties of bricks and mortar and their geometrical arrangement is still an interesting task deserving attention. One of the pioneer works on this topic is that by Hilsdorf [21], who derived the strength of the masonry for a staking sequence of bricks and mortar layers based on simplified kinematic hypotheses. Results of monotonic and cyclic uniaxial compressive tests on natural stone and clay bricks specimens, as well as natural stone and clay brick prisms have been presented in [27]. The stiffness degradation evolution, the relevance of hysteretic energy dissipation and the failure modes are discussed.

More recently, an experimental investigation on the influence of mortar and brick properties and arrangement on masonry prisms and wallettes overall response has been illustrated in [18]. A further experimental and modeling study devoted to the determination of simple formulas describing the nonlinear stress-strain response of brick-mortar staking masonry has been developed in [22], performing linear regression analyses of the experimental data. A numerical study to investigate the response of brick-mortar elements has been carried out in [32], developing micromechanical three-dimensional nonlinear finite element analyses, where brick

and mortar failure has been modeled using the Willam-Warnke five-parameter criterion. The influence on the compressive strength of straw and moisture content has been experimentally investigated. A sensitivity analysis of the response of unreinforced concrete masonry made of materials with different mechanical properties and geometrical layouts has been developed in [30], where analyses have been performed adopting a three-dimensional finite element micro-modeling approach and accounting for damage and plasticity effects. An experimental investigation on masonry subjected to compression loading condition has also been performed for textures made of tuff blocks [5], defining different nonlinear stress-strain models for each loading direction to account for masonry orthotropy and describe strain-softening behavior.

This study presents a numerical model to perform fast numerical testing of masonry prisms subjected to compressive loading conditions. Masonry overall response can be deduced by applying suitable homogenization techniques, widely discussed in literature. Among others, homogenization procedures for masonry with periodic microstructure have been presented in in [2], where an enriched plane state formulation was introduced, in [6], where higher-order continuum models were adopted and in [11], where rigid or elastic blocks and viscoelastic mortar were considered. Moreover, in [10] quasi-periodic masonry was considered. Finally, in [28] non-linear static and limit analyses were performed for masonry arch bridge.

Here, the masonry prism is considered as a heterogeneous medium made of bricks and mortar joints, arranged in different textures. A simplified kinematic model is proposed, which accounts for transverse dilatation of masonry in compression that can differs for brick and mortar layers. Moreover, considering the possible presence of head joints inside the prism, an increase of the transverse deformation is introduced in correspondence to vertical mortar joints. Equilibrium equations are deduced using a variational approach and the Euler equations are derived consistently with the proposed kinematic model. The nonlinear constitutive response of bricks and mortar is modeled via Continuum Damage Mechanics [12], introducing an isotropic damage formulation. A simplified form of the Willam-Warnke criterion, originally proposed for the tri-axial failure surface of concrete-like materials [34], is adopted for both the masonry constituents.

A novel numerical procedure to solve the nonlinear evolution problems of damage variables is proposed. This is based on the collocation technique applied to an approximated form of the solution. The evolution equations are solved in the framework of backward-Euler technique. Numerical applications are carried out to validate the proposed numerical procedure, comparing the obtained results with those evaluated by a nonlocal finite element method. An investigation on the dependence of the overall response of masonry Unit Cell (UC) on the mechanical properties of mortar and brick is illustrated. Finally, a comparison with the

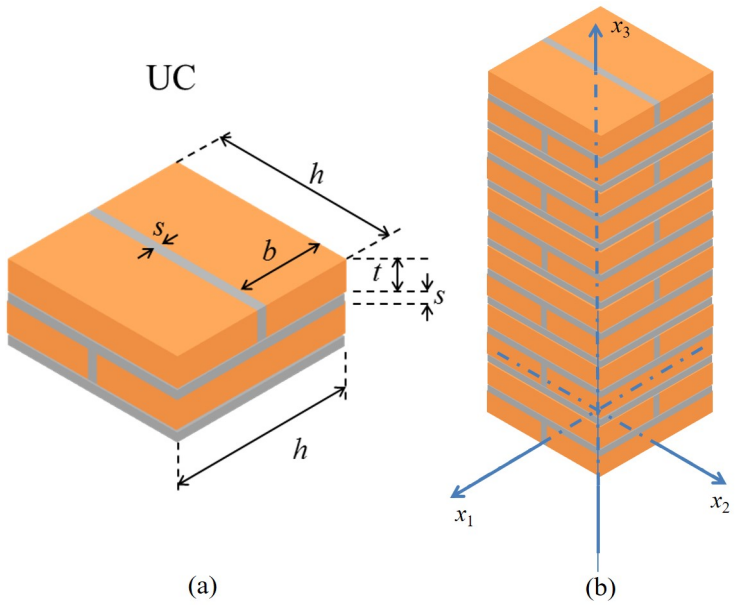

Figure 1: Schematic of the (a) UC and (b) masonry column characterized by regular periodic texture.

results of an experimental test on a masonry column is performed.

The paper is organized as follows: in Section 2 the heterogeneous masonry model is presented, proposing a simplified kinematics for the description of column response with the corresponding equilibrium equations derived via variational formulation. Section 3 illustrates the nonlinear constitutive model adopted for bricks and mortar. In Section 4 a numerical procedure based on the collocation technique is proposed. Numerical applications are described in Section 5. Finally, concluding remarks are given in Section 6.

2 Heterogeneous masonry model

A masonry column is considered, obtained as the superposition of layers composed of two bricks bonded by a vertical mortar joint and mortar layers. The brick layers, separated by the bed mortar joint, are rotated $\pi/2$ of each other. Figure 1 contains the three-dimensional scheme of the column with the Cartesian reference system set such that the x_3-axis coincides with the column axis, while x_1 and x_2 span the typical cross section of the column.

Because of the masonry texture periodicity, a single UC is studied and a homogenization procedure is used to derive the overall structural response of the masonry column. As is known, materials exhibiting strain-softening response are characterized by non-convex stored energy functionals, leading to the occurrence of localization phenomena. As a consequence of

the loss of ellipticity of the governing equations, instability phenomena can emerge at both the macroscopic and microscopic level [24, 26]. To overcome the related drawbacks, a length scale should be introduced in the standard continuum description. Various approaches can be adopted, as for example nonlocal integral, gradient and enriched continuum formulations. Relaxation techniques of the non-convex energy functional can also be adopted, based on the convexification of the stress potential [19]. In the case of a micro-macro homogenization, due to the localization phenomena the problem of the selection of a repetitive UC also emerges. Here, the selected UC in figure 1(a) is assumed to describe the possible damaging mechanisms at the micromechanical level. Possible localization problems at the macroscopic structural level can be overcome by adopting a suitable regularization technique. As shown in figure 1, the UC is composed of four bricks and two mortar bed joints arranged in four layers as follows: the first is a mortar layer, the second is made up of two bricks bonded in the $x_2 - x_3$ plane by a mortar joint, the third is a mortar layer and the fourth is composed of two bricks bonded in the $x_1 - x_3$ plane by a mortar joint. The size of the single brick is $b \times h$ and its thickness by t, while the thickness of the mortar layer is s. The UC total height is $\ell = 2\,(t + s)$. The x_3 coordinate defining the interface among the layer i and $i+1$ is denoted as ℓ_i. Moreover, it results $h = 2\,b + s$.

2.1 Kinematics

A simplified three-dimensional kinematic description is considered for the masonry UC subjected to an average axial strain E_{33}. The displacement fields are represented in the form:

$$\begin{aligned} u_1 &= x_1\, e_1(x_3) + \phi_1(x_1)\, d_1(x_3) \\ u_2 &= x_2\, e_2(x_3) + \phi_2(x_2)\, d_2(x_3) \\ u_3 &= E_{33}\, x_3 + w(x_3) \end{aligned} \quad , \tag{1}$$

where the function $\phi_i(x_i)$, with $i = 1, 2$ is defined as:

$$\phi_i(x_i) = \begin{cases} \dfrac{2\,x_i}{s} & \text{if} \quad 0 \leq |x_i| \leq \dfrac{s}{2} \\ \dfrac{h - 2\,|x_i|}{h - s}\,\mathrm{sgn}(x_i) & \text{if} \quad \dfrac{s}{2} < |x_i| \leq \dfrac{h}{2} \end{cases} \quad , \tag{2}$$

with derivative

$$\phi_{i,i}(x_i) = \begin{cases} \dfrac{2}{s} & \text{if} \quad 0 \leq |x_i| \leq \dfrac{s}{2} \\ -\dfrac{2}{h - s} & \text{if} \quad \dfrac{s}{2} < |x_i| \leq \dfrac{h}{2} \end{cases} \quad , \tag{3}$$

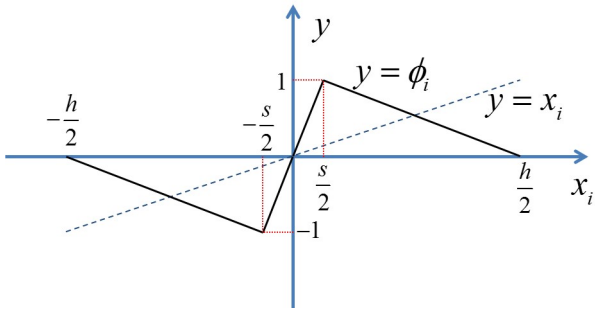

Figure 2: Shape function governing the displacement profile in the transverse direction.

the subscript '$_{,i}$' denoting the derivative with respect to x_i. The presented kinematic model is an enhancement of the enriched model proposed in [2].

In Eqs. (1), the axial displacement component is represented as additive composition of an assigned part depending on the average axial strain E_{33} and a perturbation function $w(x_3)$, arising due to medium heterogeneity, and assumed constant over the column cross-section; $e_1(x_3)$ and $e_2(x_3)$ describe the transverse dilatation occurring in the column when axially loaded, while $d_1(x_3)$ and $d_2(x_3)$ account for larger transverse dilatation in correspondence to vertical mortar joints. As the masonry column studied here is made by the repetitive superposition of UCs, the above kinematic fields $e_1(x_3)$, $e_2(x_3)$, $d_1(x_3)$, $d_2(x_3)$ and $w(x_3)$ have to satisfy periodicity conditions at boundary between the UC layers.

The function $\phi_i(x_i)$, governing the shape of the transverse deformation in vertical mortar joints, is depicted in figure 2.

The compatible strain fields, derived by the displacements in (1) are collected in the two axial and shear vectors, $\boldsymbol{\varepsilon} = \{\varepsilon_{11}\ \varepsilon_{22}\ \varepsilon_{33}\}^T$ and $\boldsymbol{\gamma} = \{\gamma_{13}\ \gamma_{23}\}^T$, respectively, expressed as:

$$\boldsymbol{\varepsilon} = \bar{\mathbf{L}}\,\boldsymbol{\eta} + \mathbf{E} = \left\{ \begin{array}{c} e_1 + \phi_{1,1}\, d_1 \\ e_2 + \phi_{2,2}\, d_2 \\ w_{,3} + E_{33} \end{array} \right\} \qquad \boldsymbol{\gamma} = \tilde{\mathbf{L}}\,\boldsymbol{\eta} = \left\{ \begin{array}{c} x_1\, e_{1,3} + \phi_1\, d_{1,3} \\ x_2\, e_{2,3} + \phi_2\, d_{2,3} \end{array} \right\}, \tag{4}$$

with $\boldsymbol{\eta} = \{e_1\ d_1\ e_2\ d_2\ w\}^T$, $\mathbf{E} = \{0\ 0\ E_{33}\}^T$ and

$$\bar{\mathbf{L}} = \begin{bmatrix} 1 & \phi_{1,1} & 0 & 0 & 0 \\ 0 & 0 & 1 & \phi_{2,2} & 0 \\ 0 & 0 & 0 & 0 & \dfrac{\partial}{\partial x_3} \end{bmatrix} \quad \tilde{\mathbf{L}} = \begin{bmatrix} x_1 \dfrac{\partial}{\partial x_3} & \phi_1 \dfrac{\partial}{\partial x_3} & 0 & 0 & 0 \\ 0 & 0 & x_2 \dfrac{\partial}{\partial x_3} & \phi_2 \dfrac{\partial}{\partial x_3} & 0 \end{bmatrix}. \tag{5}$$

Taking into account heterogeneity of the column, in the following the kinematic field is

restricted to the four layers and denoted with the superscripts '$^{(i)}$' with $i = 1, .., 4$. Kinematic functions $e_1^{(i)}$, $e_2^{(i)}$, $d_1^{(i)}$, $d_2^{(i)}$, $w^{(i)}$ have to satisfy continuity and periodicity conditions, which are written for the typical kinematic function $f^{(i)}(x_3)$ as:

$$\begin{aligned} f^{(1)}(0) &= f^{(4)}(\ell) = f^{(4)(1)} \qquad & f^{(1)}(\ell_1) &= f^2(\ell_1) = f^{(1)(2)} \\ f^{(2)}(\ell_2) &= f^{(3)}(\ell_2) = f^{(2)(3)} \qquad & f^{(3)}(\ell_3) &= f^{(4)}(\ell_3) = f^{(3)(4)} \end{aligned} \tag{6}$$

with $\ell_1 = t$, $\ell_2 = t + s$ and $\ell_3 = 2\,t + s$, where $f^{(h)(k)}$ denotes the function common value at the boundary of layers h and k.

On the basis of the kinematics defined by Eqs. (4), it is possible to compute all the components of the UC average strain. These are determined as:

$$\begin{aligned} \bar{\varepsilon}_{11} &= \frac{1}{V} \int_A \int_0^\ell (e_1 + \phi_{1,1} d_1)\; dx_3 dA = \frac{1}{\ell} \int_0^\ell e_1\, dx_3 \\ \bar{\varepsilon}_{22} &= \frac{1}{V} \int_A \int_0^\ell (e_2 + \phi_{2,2} d_2)\; dx_3 dA = \frac{1}{\ell} \int_0^\ell e_2\, dx_3 \\ \bar{\varepsilon}_{33} &= \frac{1}{V} \int_A \int_0^\ell (w_{,3} + E_{33})\; dx_3 dA = E_{33} \\ \bar{\gamma}_{13} &= \frac{1}{V} \int_A \int_0^\ell (x_1 e_{1,3} + \phi_1 d_{1,3})\; dx_3 dA = 0 \\ \bar{\gamma}_{23} &= \frac{1}{V} \int_A \int_0^\ell (x_2 e_{2,3} + \phi_2 d_{2,3})\; dx_3 dA = 0 \end{aligned} \tag{7}$$

where periodicity of functions $e_1^{(i)}$, $e_2^{(i)}$, $d_1^{(i)}$, $d_2^{(i)}$ and $w^{(i)}$ given by the first of Eqs. (6) is taken into account. To be noted that transversal strains have non zero average. Thus, vector $\mathbf{E}$ does not contain overall strains, as only the third component represents an average strain.

The matrices $\bar{\mathbf{L}}$ and $\tilde{\mathbf{L}}$ can be written as:

$$\bar{\mathbf{L}} = \bar{\mathbf{L}}^p\, \bar{\mathbf{L}}^3 \qquad \tilde{\mathbf{L}} = \tilde{\mathbf{L}}^p\, \tilde{\mathbf{L}}^3 \tag{8}$$

with

$$\bar{\mathbf{L}}^p = \begin{bmatrix} 1 & \phi_{1,1} & 0 & 0 & 0 \\ 0 & 0 & 1 & \phi_{2,2} & 0 \\ 0 & 0 & 0 & 0 & 1 \end{bmatrix} \qquad \bar{\mathbf{L}}^3 = \begin{bmatrix} 1 & 0 & 0 & 0 & 0 \\ 0 & 1 & 0 & 0 & 0 \\ 0 & 0 & 1 & 0 & 0 \\ 0 & 0 & 0 & 1 & 0 \\ 0 & 0 & 0 & 0 & \dfrac{\partial}{\partial x_3} \end{bmatrix}$$
$$\tilde{\mathbf{L}}^p = \begin{bmatrix} x_1 & \phi_1 & 0 & 0 & 0 \\ 0 & 0 & x_2 & \phi_2 & 0 \end{bmatrix} \qquad \tilde{\mathbf{L}}^3 = \mathbf{J}\frac{\partial}{\partial x_3}\,, \tag{9}$$

and $\mathbf{J}$ the 5×5 identity matrix.

The strain component γ_{12} is neglected being equal to zero.

2.2 Equilibrium

Equilibrium equations are derived via an integral formulation. The virtual displacement equation read:

$$0 \;=\; \int_\Omega \left(\delta\boldsymbol{\varepsilon}^T\boldsymbol{\sigma} + \delta\boldsymbol{\gamma}^T\boldsymbol{\tau}\right)\, dV\,, \tag{10}$$

with Ω denoting the UC volume, $\boldsymbol{\sigma} = \{\sigma_{11}\ \sigma_{22}\ \sigma_{33}\}^T$ being the axial stress vector and $\boldsymbol{\tau} = \{\tau_{13}\ \tau_{23}\}^T$ the shear stress vector.

Taking into account formulas (8) and setting $\Omega = A\,\ell$, with A the area of the column cross-section, the equilibrium equation (10) becomes:

$$\begin{aligned} 0 \;&=\; \int_\Omega \left[(\bar{\mathbf{L}}^3\,\delta\boldsymbol{\eta})^T(\bar{\mathbf{L}}^p)^T\boldsymbol{\sigma} + (\tilde{\mathbf{L}}^3\,\delta\boldsymbol{\eta})^T(\tilde{\mathbf{L}}^p)^T\boldsymbol{\tau}\right] dV \\ &=\; \int_\ell \left[(\bar{\mathbf{L}}^3\,\delta\boldsymbol{\eta})^T \int_A (\bar{\mathbf{L}}^p)^T\boldsymbol{\sigma}\, dA + (\tilde{\mathbf{L}}^3\,\delta\boldsymbol{\eta})^T \int_A (\tilde{\mathbf{L}}^p)^T\boldsymbol{\tau}\, dA\right] dx_3 \\ &=\; \int_\ell \left[(\bar{\mathbf{L}}^3\,\delta\boldsymbol{\eta})^T\mathbf{N} + (\tilde{\mathbf{L}}^3\,\delta\boldsymbol{\eta})^T\mathbf{T}\right] dx_3 \end{aligned} \tag{11}$$

where

$$\mathbf{N} = \int_A (\bar{\mathbf{L}}^p)^T\boldsymbol{\sigma}\, dA = \begin{Bmatrix} N_{11} \\ R_{11} \\ N_{22} \\ R_{22} \\ N_{33} \end{Bmatrix} \qquad \mathbf{T} = \int_A (\tilde{\mathbf{L}}^p)^T\boldsymbol{\tau}\, dA = \begin{Bmatrix} M_{13} \\ R_{13} \\ M_{23} \\ R_{23} \\ 0 \end{Bmatrix} \tag{12}$$

Vectors $\mathbf{N}$ and $\mathbf{T}$ collect generalized stress components, with N_{11}/A and N_{22}/A representing average stresses in the UC cross section, N_{33} the stress resultant in the axial direction, M_{13}

and M_{23} the moments of the shear stresses τ_{13} and τ_{23}, respectively. The four additional components, R_{11}, R_{22}, R_{13} and R_{23} are work-conjugate to the enhanced strain terms depending on the functions $\phi_i(x_i)$ and their derivatives. Indeed, these represent higher order stress resultants arising due to proposed kinematics and, accordingly to this, describe stresses in the UC cross-section. Higher order stress resultants, characterized by not direct mechanical interpretation, can be found in many higher order shell formulations based on enriched kinematics (e.g. third-order or layerwise shell models).

Integrating by parts and introducing continuity and periodicity conditions (6) into the equilibrium equation (11), it results:

$$\begin{aligned} 0 \;=\; & \sum_{i=1}^{4} \int_{\ell_i} (\delta\boldsymbol{\eta}^{(i)})^T \left(\bar{\mathbf{L}}^{3\star} \mathbf{N}^{(i)} + \tilde{\mathbf{L}}^{3\star} \mathbf{T}^{(i)} \right) dx_3 \\ & + \left(N_{33}^{(4)}(\ell) - N_{33}^{(1)}(0) \right) \delta w^{(4)(1)} + \sum_{i=1}^{3} \left(N_{33}^{(i)}(\ell_i) - N_{33}^{(i+1)}(\ell_i) \right) \delta w^{(i)(i+1)} \\ & + \left(\mathbf{T}^{(4)}(\ell) - \mathbf{T}^{(1)}(0) \right) \delta\boldsymbol{\eta}^{(4)(1)} + \sum_{i=1}^{3} \left(\mathbf{T}^{(i)}(\ell_i) - \mathbf{T}^{(i+1)}(\ell_i) \right) \delta\boldsymbol{\eta}^{(i)(i+1)} \end{aligned} \tag{13}$$

where

$$\bar{\mathbf{L}}^{3\star} = \begin{bmatrix} 1 & 0 & 0 & 0 & 0 \\ 0 & 1 & 0 & 0 & 0 \\ 0 & 0 & 1 & 0 & 0 \\ 0 & 0 & 0 & 1 & 0 \\ 0 & 0 & 0 & 0 & -\dfrac{\partial}{\partial x_3} \end{bmatrix} \qquad \tilde{\mathbf{L}}^{3\star} = -\mathbf{J}\frac{\partial}{\partial x_3} \tag{14}$$

From Eq. (13) the equilibrium equations for each layer result as:

$$\mathbf{0} = \bar{\mathbf{L}}^{3\star} \mathbf{N}^{(i)} + \tilde{\mathbf{L}}^{3\star} \mathbf{T}^{(i)} \qquad \Rightarrow \qquad \begin{cases} 0 &= N_{11}^{(i)} - M_{13,3}^{(i)} \\ 0 &= R_{11}^{(i)} - R_{13,3}^{(i)} \\ 0 &= N_{22}^{(i)} - M_{23,3}^{(i)} \\ 0 &= R_{22}^{(i)} - R_{23,3}^{(i)} \\ 0 &= N_{33,3}^{(i)} \end{cases} \tag{15}$$

with $i = 1, .., 4$, together with the boundary conditions:

$$\begin{aligned} & N_{33}^{(4)}(\ell) = N_{33}^{(1)}(0) \qquad && N_{33}^{(i)}(\ell_i) = N_{33}^{(i+1)}(\ell_i) \quad i = 1,2,3 \\ & \mathbf{T}^{(4)}(\ell) = \mathbf{T}^{(1)}(0) \qquad && \mathbf{T}^{(i)}(\ell_i) = \mathbf{T}^{(i+1)}(\ell_i) \quad i = 1,2,3 \end{aligned} \tag{16}$$

Taking into account the definitions (12) and the boundary conditions (16), the average stresses are computed as:

$$\begin{aligned}
\bar{\sigma}_{11} &= \frac{1}{V}\int_A\int_0^\ell \sigma_{11}\,dx_3dA = \frac{1}{V}\int_0^\ell N_{11}\,dx_3 = \frac{1}{V}\int_0^\ell M_{13,3}\,dx_3 = 0\\
\bar{\sigma}_{22} &= \frac{1}{V}\int_A\int_0^\ell \sigma_{22}\,dx_3dA = \frac{1}{V}\int_0^\ell N_{22}\,dx_3 = \frac{1}{V}\int_0^\ell M_{23,3}\,dx_3 = 0\\
\bar{\sigma}_{33} &= \frac{1}{V}\int_A\int_0^\ell \sigma_{33}\,dx_3dA = \frac{1}{V}\int_0^\ell N_{33}\,dx_3 = \frac{1}{A}N_{33}\,.
\end{aligned} \tag{17}$$

The proof that shear stresses have zero averages is given in the following.

3 Constitutive laws

Constitutive equations based on Continuum Damage Mechanics (CDM) are introduced for mortar and bricks, that account for the typical degradation mechanisms in the two masonry constituents. The same constitutive formulation is introduced for the two components, as both are cohesive materials exhibiting a similar mechanical response, but with different values of the governing parameters.

An isotropic elastic-damage model is considered, written in the form:

$$\boldsymbol{\sigma} = (1-D)\;\mathbf{C}\boldsymbol{\varepsilon}\,, \qquad \boldsymbol{\tau} = (1-D)\;\mu\boldsymbol{\gamma}\,, \tag{18}$$

where D is the damage variable, with $0 \le D \le 1$ and $\dot{D} \ge 0$, $\mathbf{C}$ is the 3×3 isotropic elastic constitutive matrix:

$$\mathbf{C} = \begin{bmatrix} \lambda+2\mu & \lambda & \lambda \\ \lambda & \lambda+2\mu & \lambda \\ \lambda & \lambda & \lambda+2\mu \end{bmatrix}, \tag{19}$$

with λ and μ being the Lamè constants.

To be noted that, accounting for the shear constitutive equation in (18), it results that, as the average shear strains $\bar{\gamma}_{13}$ and $\bar{\gamma}_{23}$ are zeros, the corresponding overall shear stresses vanish.

The proposed model is based on an isotropic damage model. Indeed, anisotropic damage models would be more accurate in describing the damaging mechanisms of brittle-like materials [13, 20], especially when these are characterized by regular arrangement of the microstructure

[7]. However for irregular and random microstructured materials, such as concrete and mortar, isotropic damage formulations have been suitably adopted to reproduce the degrading effects in the material constitutive response [1, 14, 23, 33]. On the other hand, anisotropic damage models are governed by many material parameters that, often, are very difficult to identify. Moreover, anisotropy of the material behavior is reproduced even by isotropic damage models by development and subsequent localization of damage. An interesting comparative discussion of the implications of isotropic and anisotropic damage modelling can be found in [16].

Dual frameworks can be adopted for CDM formulations, that is strain- and stress-based models are derived [29], both consistent with the Clausius-Duhem inequality. Accordingly, damage criteria can be stated in the strain and stress space, respectively.

Here, damage evolution is assumed to depend on the six-component effective stress vector, defined as:

$$\bar{\boldsymbol{\sigma}} = \frac{1}{1-D} \left\{ \begin{array}{c} \boldsymbol{\sigma} \\ \boldsymbol{\tau} \\ 0 \end{array} \right\} . \tag{20}$$

A simplified form of the Willam-Warnke criterion, originally proposed for the tri-axial failure surface of concrete-like materials [34], is adopted for both masonry constituents, together with an exponential damage evolution law. As suggested by [8] and following a phenomenological approach to describe the constitutive response of quasi-brittle materials, such as bricks and mortar, no distinction is drawn between yield, damage and failure surface. All are based on the definition of a stress space bounded by a limit stress locus. The modified form of the Willam-Warnke [34] yield criterion is governed by the uni-axial tensile and compressive elastic limit stresses σ_t and σ_c, respectively, usually differing from the maximum tensile and compressive stresses $\sigma_{t\,\max}$ and $\sigma_{c\,\max}$. The following quantities are introduced:

$$z = \frac{\sigma_t}{\sigma_c} \qquad r_c = \frac{z\sqrt{30}}{15\,z+5} \qquad r_t = \frac{\sqrt{30}\,z}{10} , \tag{21}$$

$$\begin{array}{rcl} u_t & = & 2\,r_c\,(r_c^2 - r_t^2)\,\cos\theta \\ v_t & = & r_c\,(2\,r_t - r_c)\,\sqrt{4\,(r_c^2 - r_t^2)\cos^2\theta + 5\,r_t^2 - 4\,r_t\,r_c} \\ w_t & = & 4\,(r_c^2 - r_t^2)\,\cos^2\theta + (r_c - 2\,r_t)^2 \end{array} . \tag{22}$$

Then, the effective equivalent stress is defined as:

$$\bar{\sigma}_{eq} = \frac{1}{3} I_1 + \sqrt{\frac{2\,J_2}{5}} \frac{z\,w_t}{u_t + v_t}\,, \tag{23}$$

where I_1 is the first invariant of the effective stress and J_2 the second invariant of the deviatoric effective stress $\bar{\boldsymbol{\sigma}}$. Finally, damage activation function, describing the elastic limit domain, is written as:

$$F = \bar{\sigma}_{eq} - \sigma_t \leq 0\,. \tag{24}$$

Damage evolution is governed by a constrained exponential law, expressed as:

$$D = \max_{history} \left\{0, \min\left\{\widetilde{D}, 1\right\}\right\}\,, \tag{25}$$

with

$$\widetilde{D} = 1 - \exp\left[\alpha(\sigma_t - \bar{\sigma}_{eq})\right]\,, \tag{26}$$

where α depends on the material strength and fracture energy.

Although the same damage evolution law governs the material response for tensile and compressive stresses, the non symmetric behavior is accounted for by properly setting mechanical parameters σ_t, σ_c and α. Indeed, different values are introduced for α, when material is mainly in tension ($\alpha = \alpha_t$) and compression ($\alpha = \alpha_c$), assuming the equivalent stress first invariant as the gauge to check whether the material is subjected to prevailing tensile or compressive stresses.

Material parameters governing the uni-axial response can be deduced via classical laboratory tests. In fact, from the experimental stress-strain curves, strength, $\sigma_{\bullet\,\max}$, and damage energy, $G_\bullet$, with $_\bullet$ equal to $_t$ or $_c$, can be deduced. Therefore, the uni-axial stress-strain law for a monotonic loading history results as:

$$\sigma = \exp\left[\alpha(\sigma_t - \bar{\sigma}_{eq})\right] E\,\varepsilon\,. \tag{27}$$

Accordingly, the values of $\sigma_\bullet$ and $\alpha_\bullet$ can be determined by solving the following two equations:

$$\begin{aligned} \sigma_{\bullet\,\max} &= \max|\sigma|\,, \\ G_\bullet &= \int |\sigma|\; d\varepsilon\,, \end{aligned} \tag{28}$$

where the integral is performed in the positive (G_t) or negative (G_c) strain field. Eqs. (28)

		brick			mortar				
		b1	b2	b3	m1	m2	m3	m4	m5
E	[MPa]	18000			1000				
ν		0.10			0.10				
σ_t	[MPa]	3.00			0.40				
$\sigma_{t\,\max}$	[MPa]	3.00			0.40				
α_t	$[\text{MPa}]^{-1}$	0.50			4.00				
G_t	[MPa]	8.06×10^{-4}			2.55×10^{-4}				
σ_c	[MPa]	9.80	25.50	26.00	4.50	4.90	5.00	3.50	7.00
$\sigma_{c\,\max}$	[MPa]	26.00	26.00	26.00	5.00	5.00	5.00	3.54	7.15
α_c	$[\text{MPa}]^{-1}$	0.05	0.28	0.50	1.50	2.00	2.20	2.00	2.00
G_c	[MPa]	0.235	0.112	0.061	0.090	0.076	0.071	0.040	0.136
η		1.00			1.00				

Table 1: Material properties for the brick and mortar. Three and five different sets of compressive material properties are introduced for the brick and mortar, respectively.

are nonlinear and can be solved numerically.

To avoid a sharp variation of the material parameters during computation, a smoothing regularization law is introduced to switch from α_t to α_c and vice-versa. Let the quantity $\bar{I}_1 = \sigma_t - \sigma_c$ be introduced, the variation of α is assumed to be ruled by:

$$\alpha = \alpha_t + \frac{1}{1 + \exp\left[\eta\left(I_1 - \bar{I}_1\right)\right]}\left(\alpha_c - \alpha_t\right) , \tag{29}$$

where η governs the rate of variation of α.

In figure 3, the brick stress-strain uni-axial constitutive law is depicted, considering three different set of material properties. The adopted material data are contained in table 1, considering three different sets for the brick compressive response, characterized by the same maximum compression strength, but different compressive damage energy. Tensile behavior is not influenced by the compressive parameters and is the same for the different settings.

Figures 4 and 5 contain the limit domain represented in the effective stress and strain spaces for the full three-dimensional and plane stress case, respectively. These correspond to the set of brick parameters b2 in table 1.

4 Solution technique

A numerical solution technique is proposed to evaluate the nonlinear response of the masonry column. In particular, to facilitate the computations and obtain a fast procedure for

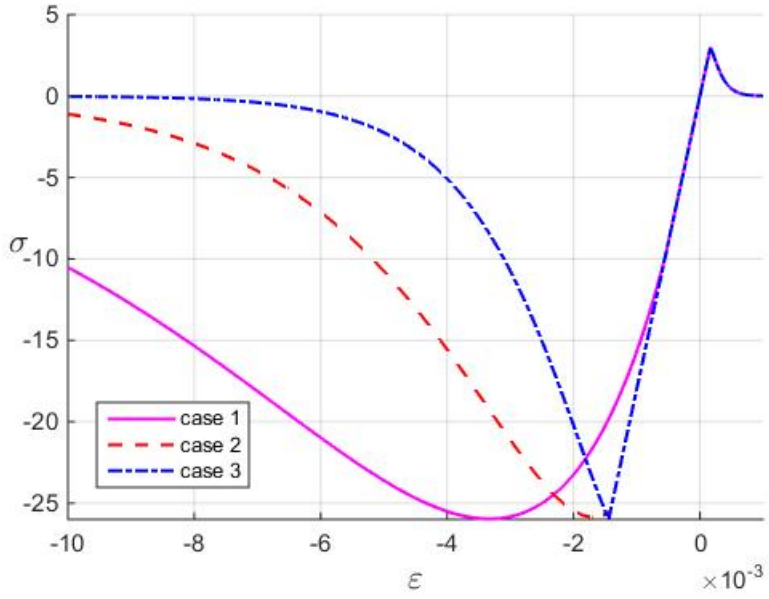

Figure 3: Stress vs strain response of the cohesive material subjected to independent tensile and compressive loading histories.

performing parametric analyses, the following main assumptions are introduced:

- damage is considered constant in the whole brick;
- the four bricks composing the masonry UC are subjected to the same damage state D_b;
- damage of the bed mortar joint is assumed constant in the whole layer;
- the two mortar layers composing the masonry UC are subjected to the same damage state D_m;
- damage of the head mortar joint is assumed constant in the whole joint;
- the two mortar joints in the masonry UC are subjected to the same damage state D_h.

The simplified hypotheses introduced gare schematically shown in figure 6(a).
Taking into account compatibility equations (4), formulas (8) and expressions of the stresses from constitutive equation (18), stress resultants (12) can be evaluated in each layer as:

$$\mathbf{N}^{(i)} = \int_{A^{(i)}} \left(1 - D^{(i)}\right) (\bar{\mathbf{L}}^p)^T \, \mathbf{C}^{(i)} (\bar{\mathbf{L}}^p \, \bar{\mathbf{L}}^3 \, \boldsymbol{\eta}^{(i)} + \mathbf{E}) \, dA = \bar{\mathbf{M}}^{(i)} \, \bar{\mathbf{L}}^3 \, \boldsymbol{\eta}^{(i)} + \bar{\mathbf{P}}^{(i)} \, \mathbf{E} \tag{30}$$

$$\mathbf{T}^{(i)} = \int_{A^{(i)}} \left(1 - D^{(i)}\right) \, G^{(i)} (\tilde{\mathbf{L}}^p)^T \tilde{\mathbf{L}}^p \, \tilde{\mathbf{L}}^3 \, \boldsymbol{\eta}^{(i)} \, dA \qquad = \tilde{\mathbf{M}} \quad \tilde{\mathbf{L}}^3 \, \boldsymbol{\eta}^{(i)} \,, \tag{31}$$

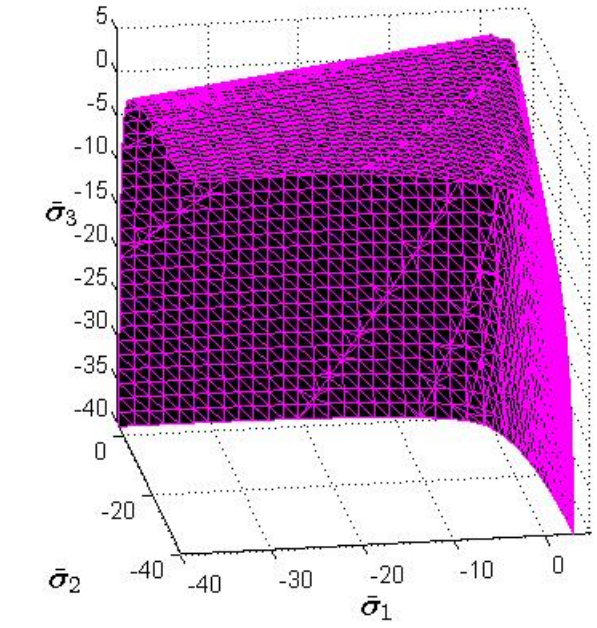

(a)

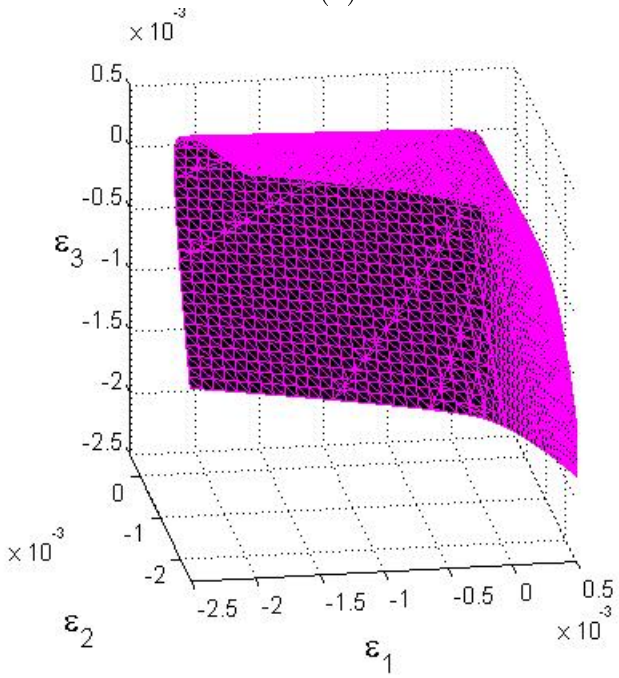

(b)

Figure 4: 3D limit domain depicted in the (a) effective stress and (b) strain space.

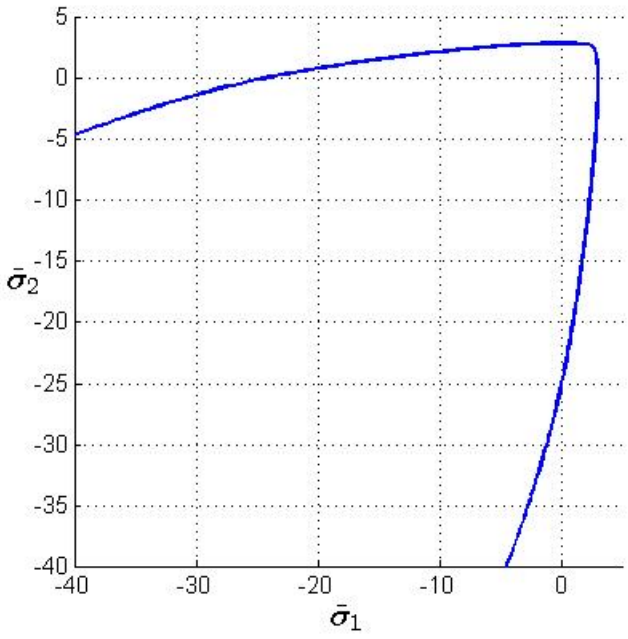

(a)

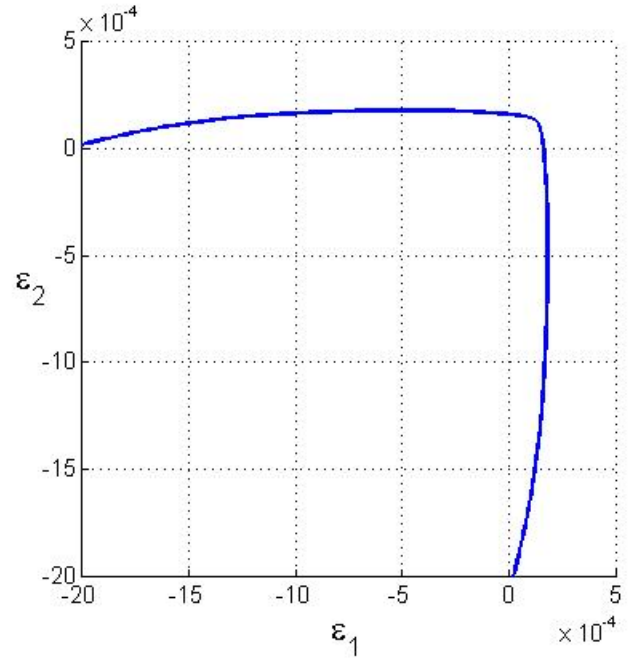

(b)

Figure 5: Limit domain for the plane stress case depicted in the (a) effective stress and (b) strain space.

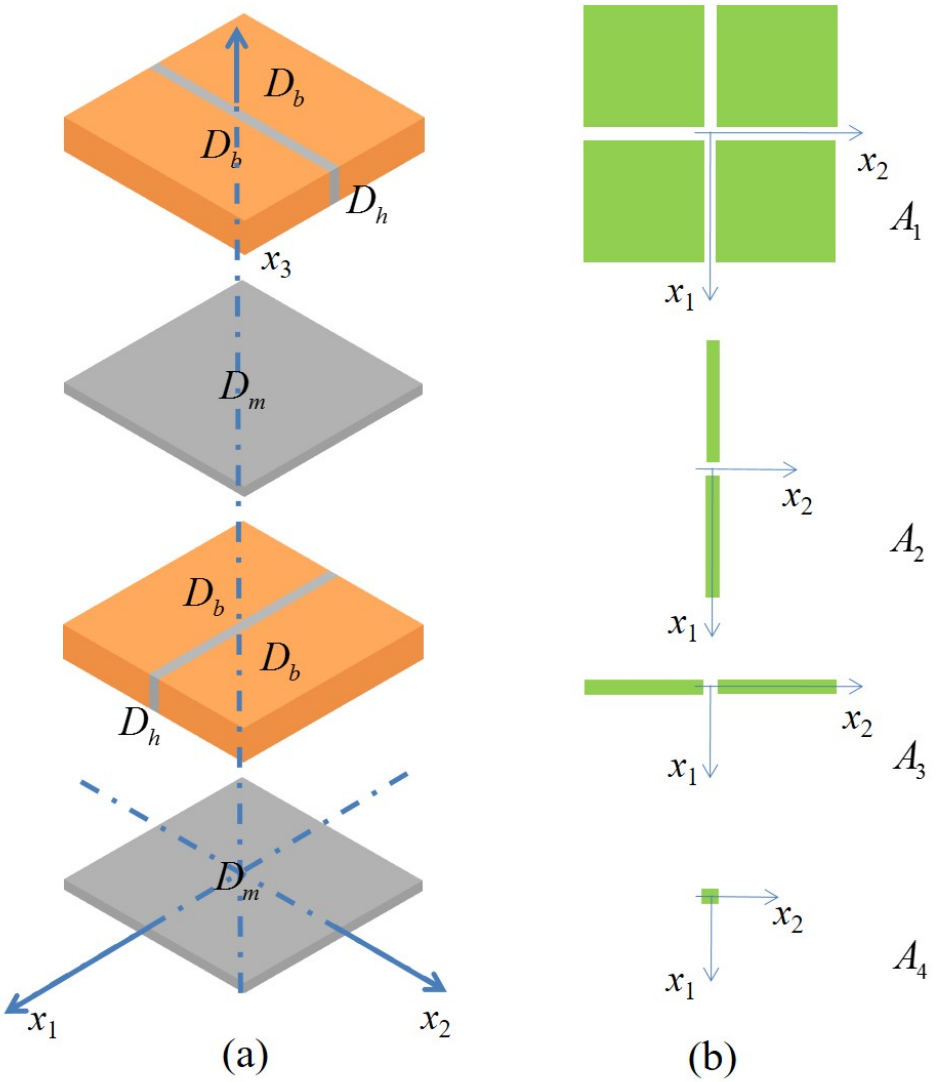

Figure 6: (a) Sequence of the four layers composing the UC; (b) areas for the strain components quadrature in the UC single layer.

where the strain vector $\mathbf{E} = \{0\ 0\ E_{33}\}^T$ contains the only assigned component E_{33}, as introduced in (4) and:

$$\bar{\mathbf{M}}^{(i)} = \sum_{j=1}^{4} \left(1 - D^{(i)\,j}\right) \bar{\mathbf{M}}^{(i)\,j} \quad \bar{\mathbf{P}}^{(i)} = \sum_{j=1}^{4} \left(1 - D^{(i)\,j}\right) \bar{\mathbf{P}}^{(i)\,j} \quad \tilde{\mathbf{M}}^{(i)} = \sum_{j=1}^{4} \left(1 - D^{(i)\,j}\right) \tilde{\mathbf{M}}^{(i)\,j}\,. \tag{32}$$

Sums in formulas (32) are performed on the four areas in which each layer of the UC is subdivided, $A_1 = h_s^2$, $A_2 = s\,h_s$, $A_3 = h_s\,s$ and $A_4 = s^2$, being $h_s = h - s$, as shown in figure 6(b). The evaluation of the quantities in formulas (32) is performed according to table 2, where for each layer the material, mortar (m), brick (b) or head joint (h), composing the four areas are indicated.

	A_1	A_2	A_3	A_4
layer 1	m	m	m	m
layer 2	b	h	b	h
layer 3	m	m	m	m
layer 4	b	b	h	h

Table 2: Material composing each area for each layer.

Matrices introduced in Eqs. (32) are defined as:

$$\bar{\mathbf{M}}^{(i)\,j} = \int_{A_j} (\bar{\mathbf{L}}^p)^T\, \mathbf{C}^{(i)\,j}\, \bar{\mathbf{L}}^p\, dA = \begin{bmatrix} c^{(i)}_{1\,j}\,A_j & c^{(i)}_{1\,j}\,\mathscr{I}_{1\,j} & c^{(i)}_{2\,j}\,A_j & c^{(i)}_{2\,j}\,\mathscr{I}_{2\,j} & c^{(i)}_{2\,j}\,A_j \\ c^{(i)}_{1\,j}\,\mathscr{I}_{1\,j} & c^{(i)}_{1\,j}\,\mathscr{I}_{3\,j} & c^{(i)}_{2\,j}\,\mathscr{I}_{1\,j} & c^{(i)}_{2\,j}\,\mathscr{I}_{5\,j} & c^{(i)}_{2\,j}\,\mathscr{I}_{1\,j} \\ c^{(i)}_{2\,j}\,A_j & c^{(i)}_{2\,j}\,\mathscr{I}_{1\,j} & c^{(i)}_{1\,j}\,A_j & c^{(i)}_{1\,j}\,\mathscr{I}_{2\,j} & c^{(i)}_{2\,j}\,A_j \\ c^{(i)}_{2\,j}\,\mathscr{I}_{2\,j} & c^{(i)}_{2\,j}\,\mathscr{I}_{5\,j} & c^{(i)}_{1\,j}\,\mathscr{I}_{2\,j} & c^{(i)}_{1\,j}\,\mathscr{I}_{4\,j} & c^{(i)}_{2\,j}\,\mathscr{I}_{2\,j} \\ c^{(i)}_{2\,j}\,A_j & c^{(i)}_{2\,j}\,\mathscr{I}_{1\,j} & c^{(i)}_{2\,j}\,A_j & c^{(i)}_{2\,j}\,\mathscr{I}_{2\,j} & c^{(i)}_{1\,j}\,A_j \end{bmatrix}, \tag{33}$$

$$\bar{\mathbf{P}}^{(i)\,j} = \int_{A_j} (\bar{\mathbf{L}}^p)^T\, \mathbf{C}^{(i)\,j}\, dA = \begin{bmatrix} c^{(i)}_{1\,j}\,A_j & c^{(i)}_{2\,j}\,A_j & c^{(i)}_{2\,j}\,A_j \\ c^{(i)}_{1\,j}\,\mathscr{I}_{1\,j} & c^{(i)}_{2\,j}\,\mathscr{I}_{1\,j} & c^{(i)}_{2\,j}\,\mathscr{I}_{1\,j} \\ c^{(i)}_{2\,j}\,A_j & c^{(i)}_{1\,j}\,A_j & c^{(i)}_{2\,j}\,A_j \\ c^{(i)}_{2\,j}\,\mathscr{I}_{2\,j} & c^{(i)}_{1\,j}\,\mathscr{I}_{2\,j} & c^{(i)}_{2\,j}\,\mathscr{I}_{2\,j} \\ c^{(i)}_{2\,j}\,A_j & c^{(i)}_{2\,j}\,A_j & c^{(i)}_{1\,j}\,A_j \end{bmatrix}, \tag{34}$$

$$\tilde{\mathbf{M}}^{(i)\,j} = G^{(i)\,j} \int_{A_j} (\tilde{\mathbf{L}}^p)^T \tilde{\mathbf{L}}^p \, dA = G^{(i)\,j} \begin{bmatrix} \mathscr{I}_{6\,j} & \mathscr{I}_{7\,j} & 0 & 0 & 0 \\ \mathscr{I}_{7\,j} & \mathscr{I}_{8\,j} & 0 & 0 & 0 \\ 0 & 0 & \mathscr{I}_{9\,j} & \mathscr{I}_{10\,j} & 0 \\ 0 & 0 & \mathscr{I}_{10\,j} & \mathscr{I}_{11\,j} & 0 \\ 0 & 0 & 0 & 0 & 0 \end{bmatrix} . \tag{35}$$

The quantities introduced in matrices (33), (34) and (35) are computed making reference to figure 6(b) and are collected in table 3.

	$j=1$	$j=2$	$j=3$	$j=4$
$\mathscr{I}_{1\,j} = \int_{A_j} \phi_{1,1} dA =$	$-2h_s$	$-2s$	$2h_s$	$2s$
$\mathscr{I}_{2\,j} = \int_{A_j} \phi_{2,2} dA =$	$-2h_s$	$2h_s$	$-2s$	$2s$
$\mathscr{I}_{3\,j} = \int_{A_j} \phi_{1,1}^2 dA =$	4	$\frac{4\,s}{h_s}$	$\frac{4\,h_s}{s}$	4
$\mathscr{I}_{4\,j} = \int_{A_j} \phi_{2,2}^2 dA =$	4	$\frac{4\,h_s}{s}$	$\frac{4\,s}{h_s}$	4
$\mathscr{I}_{5\,j} = \int_{A_j} \phi_{1,1}\phi_{2,2} dA =$	4	-4	-4	4
$\mathscr{I}_{6\,j} = \int_{A_j} x_1^2 dA =$	$\frac{(h^2+h\,s+s^2)h_s^2}{12}$	$\frac{(h^2+h\,s+s^2)h_s s}{12}$	$\frac{h_s s^3}{12}$	$\frac{s^4}{12}$
$\mathscr{I}_{7\,j} = \int_{A_j} x_1\phi_1 dA =$	$\frac{(h+2s)h_s^2}{12}$	$\frac{(h+2s)h_s s}{12}$	$\frac{h_s s^2}{6}$	$\frac{s^3}{6}$
$\mathscr{I}_{8\,j} = \int_{A_j} \phi_1^2 dA =$	$\frac{h_s^2}{3}$	$\frac{h_s s}{3}$	$\frac{h_s s}{3}$	$\frac{s^2}{3}$
$\mathscr{I}_{9\,j} = \int_{A_j} x_2^2 dA =$	$\frac{(h^2+h\,s+s^2)h_s^2}{12}$	$\frac{h_s s^3}{12}$	$\frac{(h^2+h\,s+s^2)h_s s}{12}$	$\frac{s^4}{12}$
$\mathscr{I}_{10\,j} = \int_{A_j} x_2\phi_2 dA =$	$\frac{(h+2s)h_s^2}{12}$	$\frac{h_s s^2}{6}$	$\frac{(h+2s)h_s s}{12}$	$\frac{s^3}{6}$
$\mathscr{I}_{11\,j} = \int_{A_j} \phi_2^2 dA =$	$\frac{h_s^2}{3}$	$\frac{h_s s}{3}$	$\frac{h_s s}{3}$	$\frac{s^2}{3}$

Table 3: Values of the integrals involved in the computation of the stress resultants.

Substituting expressions (30) and (31) into equilibrium equations (15), a set of 20 nonlinear differential equations, 5 for each of the 4 layers, is obtained, depending on the kinematic unknowns.

An approximated solution is then derived based on the collocation approach. In the $i-$th

layer, kinematic vector $\boldsymbol{\eta}^{(i)}$ is represented in the form:

$$\boldsymbol{\eta}^{(i)} = \hat{\boldsymbol{\eta}}^{(i)[1]}\,\psi_1^{(i)}(x_3) + \hat{\boldsymbol{\eta}}^{(i)[2]}\,\psi_2^{(i)}(x_3) + \hat{\boldsymbol{\eta}}^{(i)[3]}\,\psi_3^{(i)}(x_3) + \hat{\boldsymbol{\eta}}^{(i)[4]}\,\psi_4^{(i)}(x_3)\,, \tag{36}$$

where $\hat{\boldsymbol{\eta}}^{(i)[k]} = \left\{\hat{e}_1^{(i)[k]} \;\; \hat{d}_1^{(i)[k]} \;\; \hat{e}_2^{(i)[k]} \;\; \hat{d}_2^{(i)[k]} \;\; \hat{w}^{(i)[k]}\right\}$, with $k = 1, .., 4$, is a five component vector. Moreover, the approximation functions are set as:

$$\begin{aligned} \psi_1^{(i)} &= \frac{\ell_i - x_3}{\ell_i - \ell_{i-1}} & \psi_3^{(i)} &= \frac{4\,(x_3 - \ell_{i-1})\,(\ell_i - x_3)}{(\ell_i - \ell_{i-1})^2} \\ \psi_2^{(i)} &= \frac{x_3 - \ell_{i-1}}{\ell_i - \ell_{i-1}} & \psi_4^{(i)} &= \frac{6\sqrt{3}\,(2\,x_3 - \ell_i - \ell_{i-1})(x_3 - \ell_i)(x_3 - \ell_{i-1})}{(\ell_i - \ell_{i-1})^3} \end{aligned}\,. \tag{37}$$

Derivatives of the functions $\psi_k^{(i)}$ with respect to x_3 are:

$$\begin{aligned} \psi_{1,3}^{(i)} &= -\frac{1}{\ell_i - \ell_{i-1}} & \psi_{3,3}^{(i)} &= -\frac{4\,(2\,x_3 - \ell_{i-1} - \ell_i)}{(\ell_i - \ell_{i-1})^2} \\ \psi_{2,3}^{(i)} &= \frac{1}{\ell_i - \ell_{i-1}} & \psi_{4,3}^{(i)} &= \frac{6\,\sqrt{3}\,[6\,x_3(x_3 - \ell_i - \ell_{i-1}) + \ell_i^2 + 4\,\ell_i\ell_{i-1} + \ell_{i-1}^2]}{(\ell_i - \ell_{i-1})^3} \end{aligned} \tag{38}$$

and

$$\begin{aligned} \psi_{1,33}^{(i)} &= 0 & \psi_{3,33}^{(i)} &= -\frac{8}{(\ell_i - \ell_{i-1})^2} \\ \psi_{2,33}^{(i)} &= 0 & \psi_{4,33}^{(i)} &= \frac{36\sqrt{3}\,(2\,x_3 - \ell_i - \ell_{i-1})}{(\ell_i - \ell_{i-1})^3} \end{aligned}\,. \tag{39}$$

Figure 7 contains the plots of the approximation functions for the $i-$th layer.

Eq. (36) can be written in the equivalent form:

$$\boldsymbol{\eta}^{(i)} = \boldsymbol{\Psi}^{(i)}\,\hat{\boldsymbol{\eta}}^{(i)} \qquad \text{with } \boldsymbol{\Psi}^{(i)} = \left[\boldsymbol{\Psi}^{(i)[1]} \;\; \boldsymbol{\Psi}^{(i)[2]} \;\; \boldsymbol{\Psi}^{(i)[3]} \;\; \boldsymbol{\Psi}^{(i)[4]}\right] \qquad \hat{\boldsymbol{\eta}}^{(i)} = \left\{\begin{array}{c} \hat{\boldsymbol{\eta}}^{(i)[1]} \\ \hat{\boldsymbol{\eta}}^{(i)[2]} \\ \hat{\boldsymbol{\eta}}^{(i)[3]} \\ \hat{\boldsymbol{\eta}}^{(i)[4]} \end{array}\right\}, \tag{40}$$

being $\boldsymbol{\Psi}^{(i)[k]} = \psi_k^{(i)}\,\mathbf{J}$.

To compute stress resultants defined by Eqs. (30) and (31), the following terms have to be evaluated:

$$\bar{\mathbf{L}}^3\boldsymbol{\eta}^{(i)} = \bar{\mathbf{B}}^{(i)}\,\hat{\boldsymbol{\eta}}^{(i)} \qquad\qquad \tilde{\mathbf{L}}^3\boldsymbol{\eta}^{(i)} = \tilde{\mathbf{B}}^{(i)}\,\hat{\boldsymbol{\eta}}^{(i)}\,, \tag{41}$$

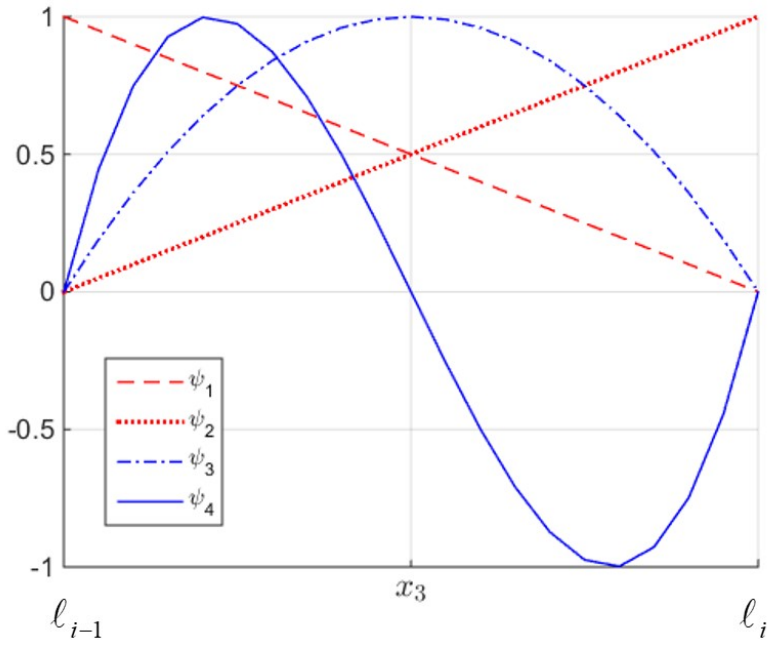

Figure 7: Plots of the selected approximation functions.

where it is set $\bar{\mathbf{B}}^{(i)} = \bar{\mathbf{L}}^3 \boldsymbol{\Psi}^{(i)}$ and $\tilde{\mathbf{B}}^{(i)} = \tilde{\mathbf{L}}^3 \boldsymbol{\Psi}^{(i)}$, resulting:

$$\bar{\mathbf{B}}^{(i)} = \left[\bar{\mathbf{B}}^{(i)[1]}\ \bar{\mathbf{B}}^{(i)[2]}\ \bar{\mathbf{B}}^{(i)[3]}\ \bar{\mathbf{B}}^{(i)[4]}\right] \qquad \text{with} \quad \bar{\mathbf{B}}^{(i)[k]} = \begin{bmatrix} \psi_k^{(i)} & 0 & 0 & 0 & 0 \\ 0 & \psi_k^{(i)} & 0 & 0 & 0 \\ 0 & 0 & \psi_k^{(i)} & 0 & 0 \\ 0 & 0 & 0 & \psi_k^{(i)} & 0 \\ 0 & 0 & 0 & 0 & \psi_{k,3}^{(i)} \end{bmatrix}, \tag{42}$$

$$\tilde{\mathbf{B}}^{(i)} = \left[\tilde{\mathbf{B}}^{(i)[1]}\ \tilde{\mathbf{B}}^{(i)[2]}\ \tilde{\mathbf{B}}^{(i)[3]}\ \tilde{\mathbf{B}}^{(i)[4]}\right] \qquad \text{with } \tilde{\mathbf{B}}^{(i)[k]} = \psi_{k,3}^{(i)}\,\mathbf{J}\,. \tag{43}$$

According to the approximation introduced (36), strain fields $\boldsymbol{\varepsilon}$ and $\boldsymbol{\gamma}$ in the $i-$th layer defined by Eqs. (4) are obtained as:

$$\boldsymbol{\varepsilon}^{(i)} = \bar{\mathbf{L}}^p\,\bar{\mathbf{B}}^{(i)}\,\hat{\boldsymbol{\eta}}^{(i)} + \mathbf{E} \qquad \boldsymbol{\gamma}^{(i)} = \tilde{\mathbf{L}}^p\,\tilde{\mathbf{B}}^{(i)}\,\hat{\boldsymbol{\eta}}^{(i)}\,. \tag{44}$$

Taking into account expressions (30) and (31) and formulas (41), the equilibrium equations (15) for the $i-$th layer take the form:

$$\left(\bar{\mathbf{L}}^{3\star}\bar{\mathbf{M}}^{(i)}\,\bar{\mathbf{B}}^{(i)} + \tilde{\mathbf{L}}^{3\star}\tilde{\mathbf{M}}^{(i)}\,\tilde{\mathbf{B}}^{(i)}\right)\hat{\boldsymbol{\eta}}^{(i)} + \bar{\mathbf{L}}^{3\star}\bar{\mathbf{P}}^{(i)}\,\mathbf{E} = \mathbf{0}\,. \tag{45}$$

Introducing matrices:

$$\bar{\mathbf{K}}^{(i)} = \left[\bar{\mathbf{K}}^{(i)\,[1]} \;\; \bar{\mathbf{K}}^{(i)\,[2]} \;\; \bar{\mathbf{K}}^{(i)\,[3]} \;\; \bar{\mathbf{K}}^{(i)\,[4]}\right] \tag{46}$$

$$\tilde{\mathbf{K}}^{(i)} = \left[\tilde{\mathbf{K}}^{(i)\,j\,[1]} \;\; \tilde{\mathbf{K}}^{(i)\,[2]} \;\; \tilde{\mathbf{K}}^{(i)\,[3]} \;\; \tilde{\mathbf{K}}^{(i)\,[4]}\right], \tag{47}$$

with

$$\begin{aligned}\bar{\mathbf{K}}^{(i)\,[k]} &= \bar{\mathbf{L}}^{3\star}\bar{\mathbf{M}}^{(i)}\,\bar{\mathbf{B}}^{(i)[k]} \\ &= \begin{bmatrix} \bar{M}^{(i)}_{11}\psi^{(i)}_{k} & \bar{M}^{(i)}_{12}\psi^{(i)}_{k} & \bar{M}^{(i)}_{13}\psi^{(i)}_{k} & \bar{M}^{(i)}_{14}\psi^{(i)}_{k} & \bar{M}^{(i)}_{15}\psi^{(i)}_{k,3} \\ \bar{M}^{(i)}_{21}\psi^{(i)}_{k} & \bar{M}^{(i)}_{22}\psi^{(i)}_{k} & \bar{M}^{(i)}_{23}\psi^{(i)}_{k} & \bar{M}^{(i)}_{24}\psi^{(i)}_{k} & \bar{M}^{(i)}_{25}\psi^{(i)}_{k,3} \\ \bar{M}^{(i)}_{31}\psi^{(i)}_{k} & \bar{M}^{(i)}_{32}\psi^{(i)}_{k} & \bar{M}^{(i)}_{33}\psi^{(i)}_{k} & \bar{M}^{(i)}_{34}\psi^{(i)}_{k} & \bar{M}^{(i)}_{35}\psi^{(i)}_{k,3} \\ \bar{M}^{(i)}_{41}\psi^{(i)}_{k} & \bar{M}^{(i)}_{42}\psi^{(i)}_{k} & \bar{M}^{(i)}_{43}\psi^{(i)}_{k} & \bar{M}^{(i)}_{44}\psi^{(i)}_{k} & \bar{M}^{(i)}_{45}\psi^{(i)}_{k,3} \\ -\bar{M}^{(i)}_{51}\psi^{(i)}_{k,3} & -\bar{M}^{(i)}_{52}\psi^{(i)}_{k,3} & -\bar{M}^{(i)}_{53}\psi^{(i)}_{k,3} & -\bar{M}^{(i)}_{54}\psi^{(i)}_{k,3} & -\bar{M}^{(i)}_{55}\psi^{(i)}_{k,33} \end{bmatrix}\end{aligned} \tag{48}$$

$$\tilde{\mathbf{K}}^{(i)\,[k]} = \tilde{\mathbf{L}}^{3\star}\tilde{\mathbf{M}}^{(i)}\,\tilde{\mathbf{B}}^{(i)[k]} = \psi_{k,33}\,\tilde{\mathbf{M}}^{(i)} \tag{49}$$

and vector:

$$\bar{\mathbf{p}}^{(i)} = \bar{\mathbf{L}}^{3\star}\bar{\mathbf{P}}^{(i)}\,\mathbf{E} = \begin{Bmatrix} \bar{P}^{(i)}_{13} \\ \bar{P}^{(i)}_{23} \\ \bar{P}^{(i)}_{33} \\ \bar{P}^{(i)}_{43} \\ 0 \end{Bmatrix} E_{33}\,, \tag{50}$$

the equilibrium equation (45) becomes

$$\mathbf{K}^{(i)}\,\hat{\boldsymbol{\eta}}^{(i)} + \mathbf{p}^{(i)} = \mathbf{0} \qquad \text{with } \mathbf{K}^{(i)} = \bar{\mathbf{K}}^{(i)\,j} + \tilde{\mathbf{K}}^{(i)\,j}\,. \tag{51}$$

Writing (51) for each of the four layers, a set of 20 equations result.

Noting that matrices $\bar{\mathbf{K}}^{(i)\,j}$ (46) and $\tilde{\mathbf{K}}^{(i)\,j}$ (47) are functions of x_3 coordinate as these depend on $\psi_k(x_3)$ and its derivatives, a collocation method is adopted to solve the micromechanical problem. Thus, Eqs. (51) are collocated in the typical i-th layer at coordinates:

$$\xi^{(i)}_1 = \ell_{i-1} + (\ell_i - \ell_{i-1})\left(\frac{1}{2} - \sqrt{\frac{3}{6}}\right) \qquad \xi^{(i)}_2 = \ell_{i-1} + (\ell_i - \ell_{i-1})\left(\frac{1}{2} + \sqrt{\frac{3}{6}}\right). \tag{52}$$

Denoting with $\mathbf{K}^{(i)}|_{\xi_s}$ the matrix $\mathbf{K}^{(i)}$ evaluated at the collocation point $x_3 = \xi^{(i)}_s$ $(s = 1, 2)$,

the collocated form of Eq. (51) is:

$$\mathbf{K}_c^{(i)}\,\hat{\boldsymbol{\eta}}^{(i)} + \mathbf{p}_c^{(i)} \qquad \text{with } \mathbf{K}_c^{(i)} = \begin{bmatrix} \mathbf{K}^{(i)}|_{\xi_1} \\ \mathbf{K}^{(i)}|_{\xi_2} \end{bmatrix} \qquad \mathbf{p}_c^{(i)} = \begin{Bmatrix} \mathbf{p}^{(i)} \\ \mathbf{p}^{(i)} \end{Bmatrix}, \tag{53}$$

corresponding to 10 algebraic equations per layer and a total of of 40 equations.

Taking into account representation form (36) for the kinematic vector in each layer and the specific choice (37) for the approximation functions ψ_k, continuity and periodicity equations for the kinematic variables (6) take the form:

$$\begin{array}{ll} \hat{\boldsymbol{\eta}}^{(1)[2]} = \hat{\boldsymbol{\eta}}^{(2)[1]} \\ \hat{\boldsymbol{\eta}}^{(2)[2]} = \hat{\boldsymbol{\eta}}^{(3)[1]} \\ \hat{\boldsymbol{\eta}}^{(3)[2]} = \hat{\boldsymbol{\eta}}^{(4)[1]} \\ \hat{\boldsymbol{\eta}}^{(4)[2]} = \hat{\boldsymbol{\eta}}^{(1)[1]} \end{array} \quad \Rightarrow \quad \begin{array}{ll} \mathbf{J}^{[2]}\hat{\boldsymbol{\eta}}^{(1)} - \mathbf{J}^{[1]}\hat{\boldsymbol{\eta}}^{(2)} = \mathbf{0} \\ \mathbf{J}^{[2]}\hat{\boldsymbol{\eta}}^{(2)} - \mathbf{J}^{[1]}\hat{\boldsymbol{\eta}}^{(3)} = \mathbf{0} \\ \mathbf{J}^{[2]}\hat{\boldsymbol{\eta}}^{(3)} - \mathbf{J}^{[1]}\hat{\boldsymbol{\eta}}^{(4)} = \mathbf{0} \\ \mathbf{J}^{[2]}\hat{\boldsymbol{\eta}}^{(4)} - \mathbf{J}^{[1]}\hat{\boldsymbol{\eta}}^{(1)} = \mathbf{0} \end{array}, \tag{54}$$

with $\mathbf{J}^{[1]} = [\mathbf{J}\ \ \mathbf{0}\ \ \mathbf{0}\ \ \mathbf{0}\ \ \mathbf{0}]$ and $\mathbf{J}^{[2]} = [\mathbf{0}\ \ \mathbf{J}\ \ \mathbf{0}\ \ \mathbf{0}\ \ \mathbf{0}]$, being $\mathbf{0}$ the 5×5 null matrix. Relationships (54) add 20 further equations to the governing set.

Equations (16), expressing stress continuity between layers composing the UC, have also to be enforced. Taking into account formulas (41), the stress resultants given in (30) and (31), become:

$$\mathbf{N}^{(i)} = \bar{\mathbf{M}}^{(i)}\,\bar{\mathbf{B}}^{(i)}\,\hat{\boldsymbol{\eta}}^{(i)} + \bar{\mathbf{P}}^{(i)}\,\mathbf{E} \tag{55}$$

$$\mathbf{T}^{(i)} = \tilde{\mathbf{M}}^{(i)}\,\tilde{\mathbf{B}}^{(i)}\,\hat{\boldsymbol{\eta}}^{(i)} \tag{56}$$

Note that Eqs. (16) involve the first four components of vectors $\mathbf{T}^{(i)}$ and the fifth component of vectors $\mathbf{N}^{(i)}$. Further 20 equations are, then, written.

Finally, the set of governing equations can be schematically organized as:

$$\begin{bmatrix} \mathbf{J}^{[2]} & -\mathbf{J}^{[1]} & \mathbf{0} & \mathbf{0} \\ \mathbf{0} & \mathbf{J}^{[2]} & -\mathbf{J}^{[1]} & \mathbf{0} \\ \mathbf{0} & \mathbf{0} & \mathbf{J}^{[2]} & -\mathbf{J}^{[1]} \\ -\mathbf{J}^{[1]} & \mathbf{0} & \mathbf{0} & \mathbf{J}^{[2]} \\ \mathbf{K}^{(1)}|_{\xi_1} & \mathbf{0} & \mathbf{0} & \mathbf{0} \\ \mathbf{K}^{(1)}|_{\xi_2} & \mathbf{0} & \mathbf{0} & \mathbf{0} \\ \mathbf{0} & \mathbf{K}^{(2)}|_{\xi_1} & \mathbf{0} & \mathbf{0} \\ \mathbf{0} & \mathbf{K}^{(2)}|_{\xi_2} & \mathbf{0} & \mathbf{0} \\ \mathbf{0} & \mathbf{0} & \mathbf{K}^{(3)}|_{\xi_1} & \mathbf{0} \\ \mathbf{0} & \mathbf{0} & \mathbf{K}^{(3)}|_{\xi_2} & \mathbf{0} \\ \mathbf{0} & \mathbf{0} & \mathbf{0} & \mathbf{K}^{(4)}|_{\xi_1} \\ \mathbf{0} & \mathbf{0} & \mathbf{0} & \mathbf{K}^{(4)}|_{\xi_2} \\ \mathbf{F}^{(1)}|_{\ell_1} & -\mathbf{F}^{(2)}|_{\ell_1} & \mathbf{0} & \mathbf{0} \\ \mathbf{0} & \mathbf{F}^{(2)}|_{\ell_2} & -\mathbf{F}^{(3)}|_{\ell_2} & \mathbf{0} \\ \mathbf{0} & \mathbf{0} & \mathbf{F}^{(3)}|_{\ell_3} & -\mathbf{F}^{(4)}|_{\ell_3} \\ -\mathbf{F}^{(1)}|_{\ell_0} & \mathbf{0} & \mathbf{0} & \mathbf{F}^{(4)}|_{\ell_4} \end{bmatrix} \begin{Bmatrix} \hat{\boldsymbol{\eta}}^{(1)} \\ \hat{\boldsymbol{\eta}}^{(2)} \\ \hat{\boldsymbol{\eta}}^{(3)} \\ \hat{\boldsymbol{\eta}}^{(4)} \end{Bmatrix} = - \begin{Bmatrix} \mathbf{0} \\ \mathbf{0} \\ \mathbf{0} \\ \mathbf{0} \\ \mathbf{p}^{(1)} \\ \mathbf{p}^{(1)} \\ \mathbf{p}^{(2)} \\ \mathbf{p}^{(2)} \\ \mathbf{p}^{(3)} \\ \mathbf{p}^{(3)} \\ \mathbf{p}^{(4)} \\ \mathbf{p}^{(4)} \\ \mathbf{q}^{(1)} - \mathbf{q}^{(2)} \\ \mathbf{q}^{(2)} - \mathbf{q}^{(3)} \\ \mathbf{q}^{(3)} - \mathbf{q}^{(4)} \\ \mathbf{q}^{(4)} - \mathbf{q}^{(1)} \end{Bmatrix} \tag{57}$$

where

$$\begin{aligned} \mathbf{F}^{(i)} &= \begin{bmatrix} \left[\tilde{\mathbf{M}}^{(i)}\, \tilde{\mathbf{B}}^{(i)}(\ell_i)\right]_{(1..4,:)} \\ \left[\bar{\mathbf{M}}^{(i)}\, \bar{\mathbf{B}}^{(i)}(\ell_i)\, \hat{\boldsymbol{\eta}}^{(i)}\right]_{(5,:)} \end{bmatrix} \\ \mathbf{q}^{(i)} &= \left\{0 \;\; 0 \;\; 0 \;\; 0 \;\; \bar{P}_{53}^{(i)}\right\}^T E_{33}\,, \end{aligned} \tag{58}$$

obtaining an algebraic system of 80 equations in 80 unknowns (i.e. 20 components of each vector $\hat{\boldsymbol{\eta}}^{(i)}$ with $i = 1, ..., 4$). To eliminate rigid body translation along x_3 direction, a further constraint equation is introduced as:

$$\hat{w}^{(4)[2]} = 0 \tag{59}$$

At the same time, the stress continuity equation $N_{33}^{(4)}(\ell) = N_{33}^{(1)}(0)$, is cut out.

The three damage variables D_b, D_m and D_h are evaluated on the basis of stresses computed at the following points in the UC:

- Q_b at $x_1 = 0,\ x_2 = (s+b)/2,\ x_3 = s + t/2$;

- Q_m at $x_1 = 0,\ x_2 = 0,\ x_3 = s/2$;
- Q_j at $x_1 = 0,\ x_2 = 0,\ x_3 = x + t/2$;

respectively.

Once unknown vector $\hat{\eta}$ is computed, the kinematic quantities arranged in vector $\eta^{(i)}$ can be evaluated for each layer at points Q_b, Q_m, Q_j, using formula (36). Thus, axial and shear strains are determined by Eqs. (44) and, using Eqs. (18) and (20), the effective stress $\bar{\sigma}$ is computed. Damage evolution at points Q_b, Q_m, Q_j is evaluated through Eqs. (21)-(26). The presented numerical procedure has been implemented in MATLAB.

5 Numerical applications

This section presents some numerical applications to validate the proposed model on the basis of the results of FE analyses and experimental outcomes. First, numerical testings on masonry columns characterized by different geometrical textures are performed, comparing the results with those obtained by nonlinear nonlocal FE analyses. A parametric investigation on the overall response of the masonry column is then conducted, varying the mechanical properties of the components. Finally, an experimental compressive test on a masonry prism is simulated.

5.1 Comparison with FE analyses

To numerically validate the model presented, the compressive response of the masonry column UC is studied. Different arrangements are considered as shown in figure 8, denoted in the following with (a) UC1, (b) UC2, (c) UC3 and (d) UC4. Head joints are not included in UC1, while in UC2 and UC3 these have a different arrangement. Moreover, UC4 is equal to UC2, but mortar is eliminated by head joints.

The following geometrical parameters are adopted: $h = 240\,\text{mm}$, $b = 115\,\text{mm}$, $t = 55\,\text{mm}$, $s = 10\,\text{mm}$. Brick and mortar constitutive response is ruled by the damage model presented in Section 3, assuming mechanical parameters in Table 1 and selecting data b2 for bricks and m2 for mortar joints. The UC response is also evaluated by FE procedure for comparison, using 3D 8-node solid elements for modeling bricks and mortar and a $2 \times 2 \times 2$ Gauss integration rule. The 3D solid element, formulated on the basis of the constitutive model in Section 3, has been implemented in the FE code FEAP [31]. To overcome mesh-dependency problems and regularize the FE numerical solution, a nonlocal integral procedure is used, introducing

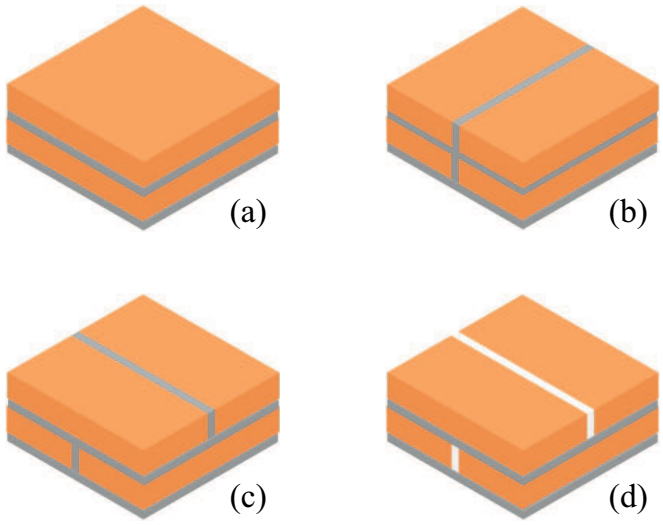

Figure 8: Masonry UC arrangements: (a) UC1, (b) UC2, (c) UC3 and (d) UC4.

in Eq. (24) the integral definition of the effective equivalent stress (23). To compare the FE results with those evaluated through the procedure presented here, which assumes constant damage in bricks and mortar joints, a high value for the nonlocal radius, that is 500 mm, is adopted. Figures 9 and 10 contain the compressive response of the four UCs, in terms of homogenized stress component Σ_{33} versus applied average axial strain E_{33}, evaluated via the proposed model (solid black line) and the FE procedure (red line with stars). A very satisfactory agreement between the two solution procedures is observed. All the analyzed cases show a very similar response, denoting that the presence of head mortar joints does not significantly influence overall UC response, as clearly emerges in figure 11(b), where responses of the four UCs are compared. Moreover, figure 11(a) shows the comparison between UC1 compressive response (solid black line) and that of a fictitious homogeneous UC only made of brick (solid red line), or mortar (solid green line). As expected, the strength and stiffness of the heterogeneous UC are average values of brick and mortar properties. As for the post-peak behavior of UC1, this is more brittle. Figure 12 shows the damage evolution in brick and bed mortar joints, evaluated with the proposed procedure (solid lines) and the FE technique (line with stars). Damage first starts in the bricks with a very steep growth, then it proceeds in the mortar bed joints. Coinciding damage evolution trends are obtained with the proposed procedure and the FE technique.

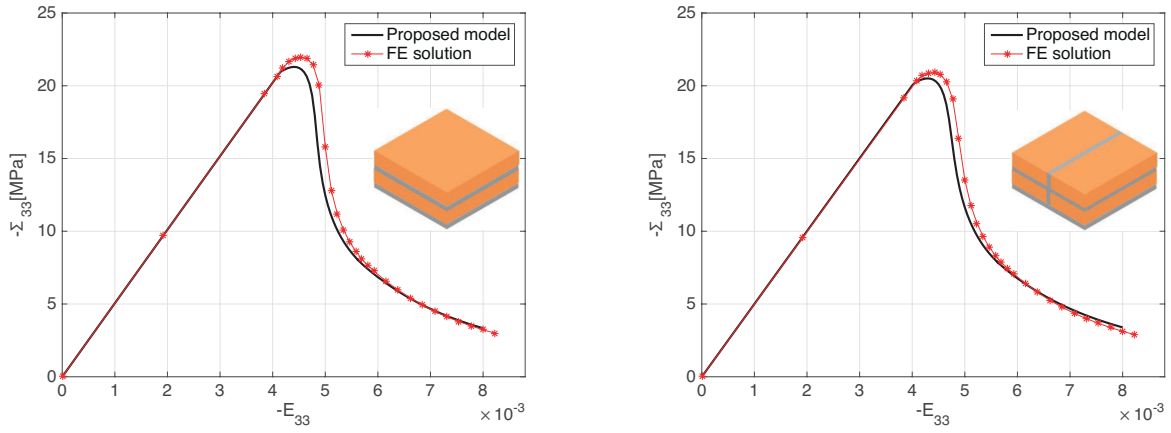

(a) (b)

Figure 9: Overall compressive stress-strain response of (a) UC1 and (b) UC2.

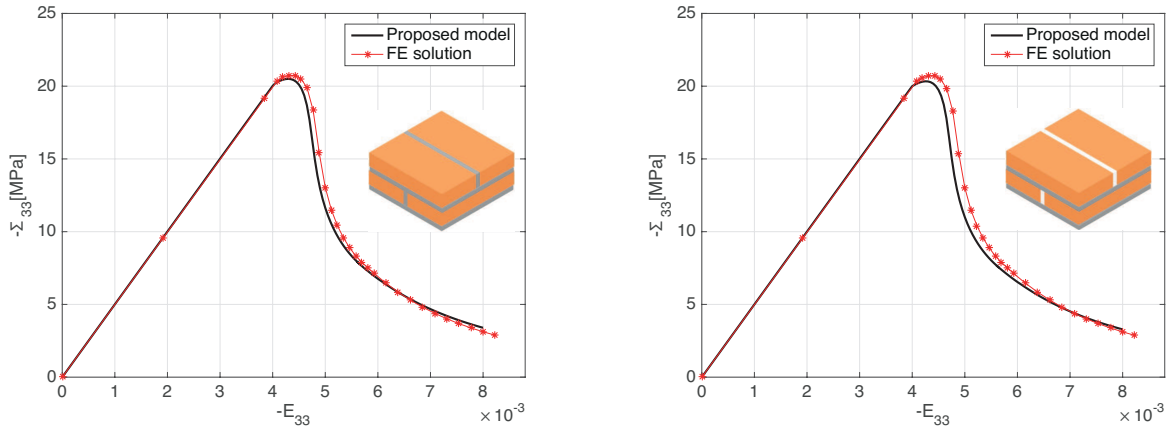

(a) (b)

Figure 10: Overall compressive stress-strain response of (c) UC3 and (d) UC4.

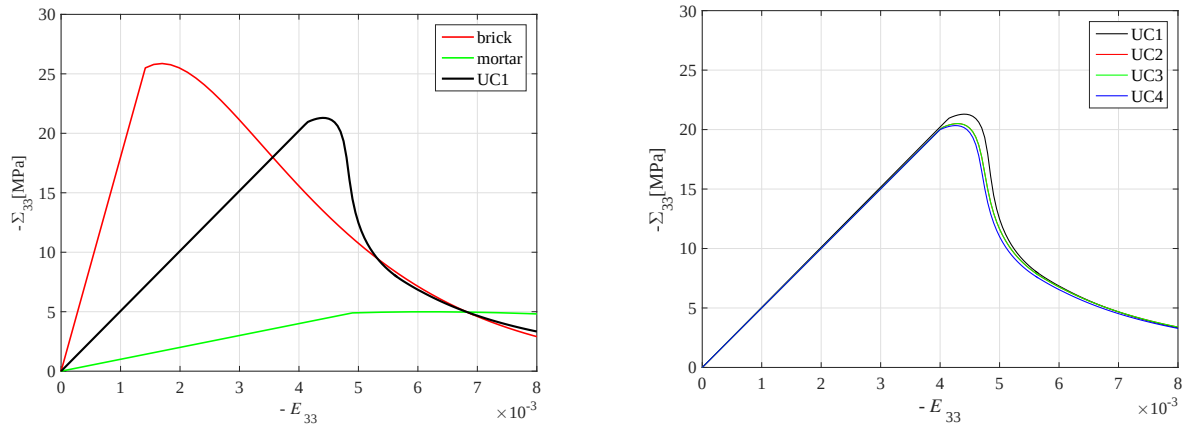

(a) (b)

Figure 11: Overall compressive stress-strain response: (a) comparison between UC1 (black), brick UC (red) and mortar UC (green); (b) comparison between the different UCs in figure 8.

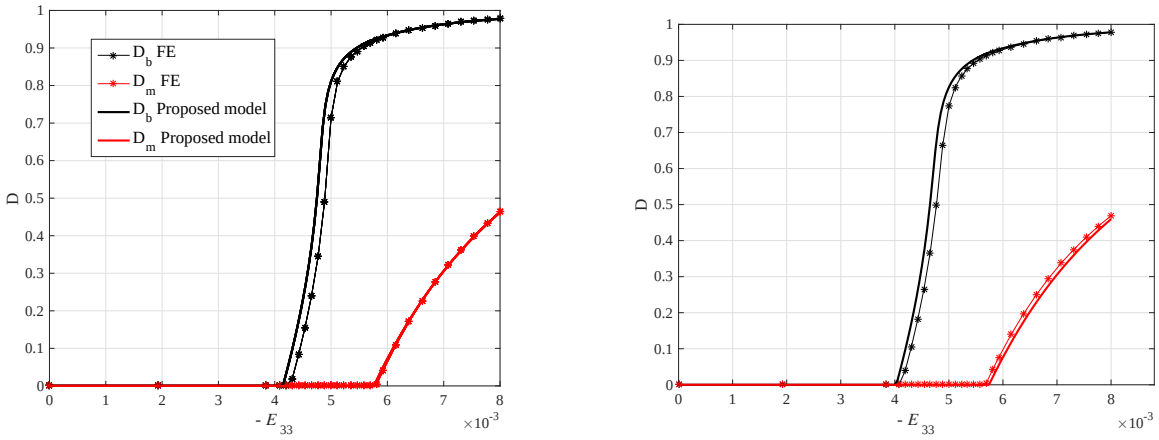

(a) (b)

Figure 12: Damage evolution in UC1 and UC2: comparison between the damage evaluated in (a) UC1 and (b) UC2 with the proposed model (solid lines) and the FE procedure (line with stars) in the brick (black) and mortar bed joint (red).

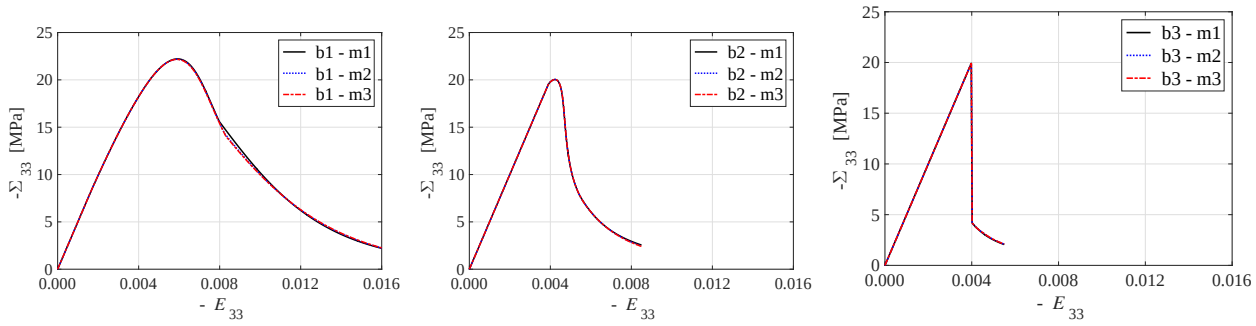

(a) (b) (c)

Figure 13: UC3 overall response considering different values of mechanical properties for brick and mortar: response of the masonry prism composed of (a) bricks b1 and mortar m1, m2 and m3, (b) bricks b2 and mortar m1, m2 and m3, (c) bricks b3 and mortar m1, m2 and m3.

5.2 Effects of mechanical properties on UC overall response

A parametric investigation is performed considering UC3 (figure 8) with geometrical parameters given in the previous section. Axes bounds are the same in Figures 13, 14, 15, that is the strain $-E_{33}$ ranges from 0 to 0.016 and the stress $-S_{33}$ from 0 to 25 MPa.

Different mechanical properties are considered for brick and mortar, as contained in table 1, where b1, b2 and b3 correspond to bricks characterized by the same maximum compressive strength but different fracture energies. As for the mortar, m1, m2, m3, m4 and m5 refer to materials differing both for maximum compressive strength and fracture energy. Figure 13 contains the overall response of UC3 made of the three different bricks (a) b1, (b) b2 and (c) b3. In each figure, the response is plotted for the three mortar materials m1, m2 and m3, having the same maximum compressive strength and different values of fracture energy. It clearly emerges that the variation of the mortar compressive fracture energy has a negligible influence on the masonry UC overall behavior. It is not possible to distinguish the curves obtained changing the mortar properties. Instead, the reduction of brick compressive fracture energy causes a lower UC strength with the peak moved backwards and an increasingly steeper softening branch. To be noted in the case of brick b3, the most brittle, a sudden post-peak drop occurs after the linear elastic response. The jump of the overall stress occurring at the strain value $E_{33} = 0.04$ is due to the performed displacement control of the analysis. Of course, following the load path via an arc-length technique, a snap back branch would be recovered.

A further investigation on the influence of the mortar mechanical properties on the masonry overall response is performed, considering mortar joints characterized by different compressive

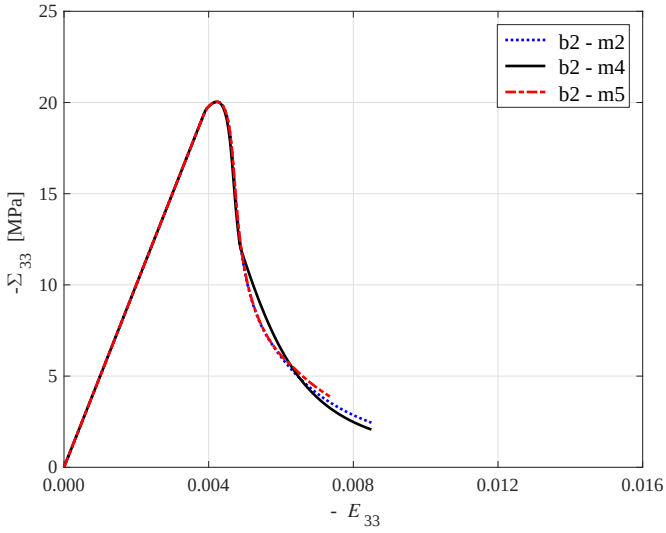

Figure 14: UC3 overall response for the different mortar materials m2, m4 and m4, and brick b2.

strengths. Mortar m2, m4 and m5 in table 1 are considered with brick b2. Note that the mortar materials are characterized by significantly different strengths, going from 3.54 to 7.15 MPa. In figure 14 overall stress versus overall strain for UC3 with the three different mortar materials is plotted. It can be noted that, although very different values of mortar strength are considered, the overall strength of the masonry prism does not change, whereas the softening branches show a slight discrepancy.

In figure 15 the response of UC3 made of bricks b1, b2 and b3 and mortar m2 is plotted. It is again confirmed that the brick mechanical properties strongly influence the overall masonry prism response. In particular, only modifying brick fracture energy a significantly different UC overall response is obtained. Indeed, in the example reported in figure 15 the use of brick b1 yields a maximum compressive strength for UC3 equal to 22.18 MPa and a fracture energy of 0.176 MPa; brick b2 a maximum compressive strength equal to 20.04 MPa with a fracture energy of 0.075 MPa; brick b3 a maximum compressive strength equal to 19.92 MPa with a fracture energy of 0.044 MPa. Note that the fracture energy is computed for an overall residual stress of about 2.5 MPa. Moreover, fracture energy is overestimated for brick b3, as no snap back is accounted for in the displacement-controlled analysis. It can be concluded that brick fracture energy strongly influences the UC strength and fracture energy .

To show the orthotropic behavior of the UC3, the plots of the lateral strains and displacements along the axis of the unit cell are reported. In particular, the lateral strain contributions e_1 and e_2 vs x_3 and d_1 and d_2 vs x_3 are reported in figures 16(a) and 16(b), respectively. From

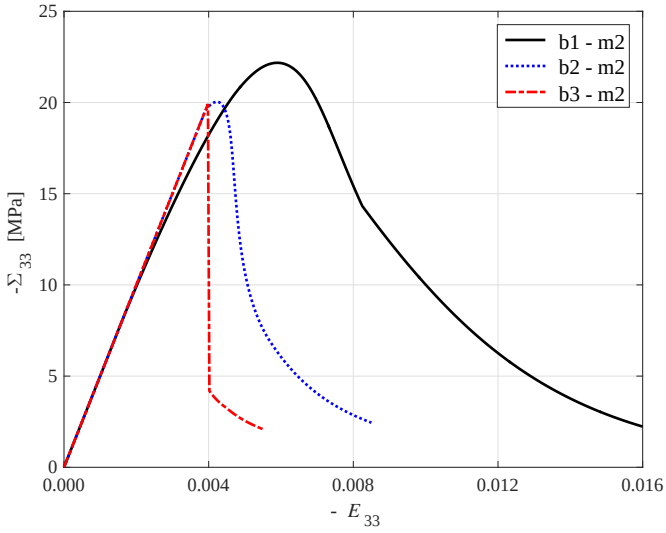

Figure 15: UC3 overall response for the different brick properties b1, b2 and b3, and mortar m2.

figure 16, the different response of the UC along the lateral directions can be noted. It can also be noted that the response of layers 1 and 2 along the x_1-direction is the same as that obtained for layers 3 and 4 along the x_2-direction, as could be expected due to the specific geometry considered for the computations. Figure 16(b) illustrates the influence of terms d_1 and d_2 in the head mortar joints. In fact, d_1 assumes significant values in correspondence to layer 4 in the head joint. Analogously, d_2 is not negligible in layer 2, again in the head joint.

Figures 17 illustrates the profiles of the displacement component u_1 and u_2 along the axis of the UC. In particular, figure 17(a) reports the lateral displacement component u_1 evaluated at $x_1 = s/2$ and at $x_1 = h/2$ Analogously, figure17(b) reports the lateral displacement component u_2 evaluated at $x_2 = s/2$ and at $x_2 = h/2$.

5.3 Comparison with an experimental test

The simulation of a compressive test for a masonry prism is performed. The analyzed column is obtained as staking sequence of four clay brick units joined by three mortar layers; two more mortar layers are present at the top and bottom of the prism, according to figure 18(a). In figure 18(b) the UC adopted for the computations is illustrated.

This structural scheme was studied both experimentally and numerically in [9], considering axial and eccentric loading conditions. A numerical investigation is also reported in [3]. The vertical load is applied to the masonry prism by means of two steel plates located in direct

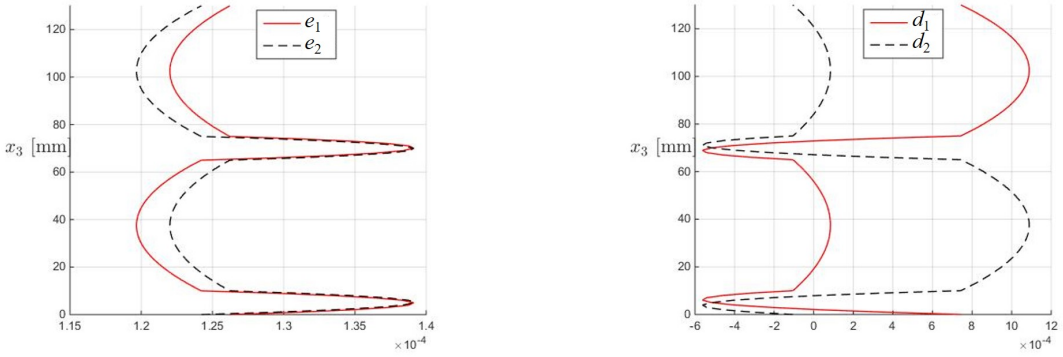

(a) (b)

Figure 16: Lateral strain contributions along the axis of the UC at $E_{33} = -0.0035$; (a) e_1 and e_2 vs x_3, (b) d_1 and d_2 vs x_3

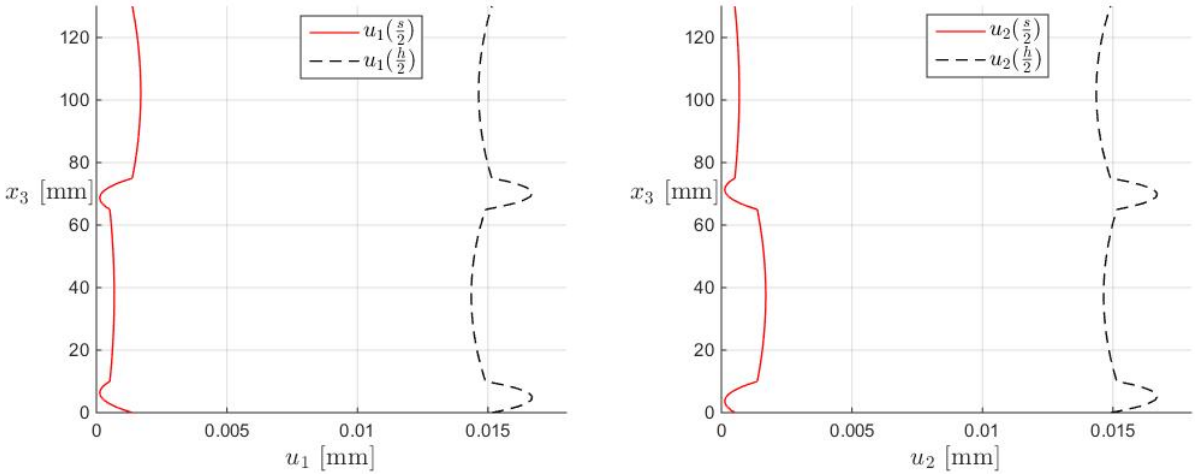

(a) (b)

Figure 17: Lateral displacements along the axis of the UC at $E_{33} = -0.0035$; (a) u_1 evaluated at $x_1 = s/$ and at $x_1 = h/2$ vs x_3, (b) u_2 evaluated at $x_2 = s/$ and at $x_2 = h/2$ vs x_3

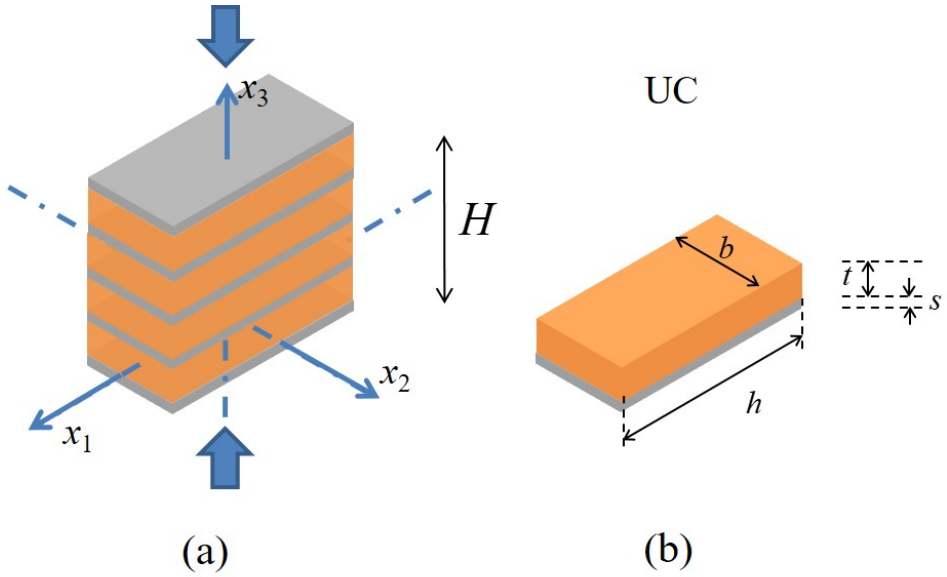

Figure 18: Axially loaded column: (a) schematic of the masonry prism, (b) UC adopted for the computations.

contact with the lower and upper mortar joints. The size of the bricks is $240 \times 55 \times 110\,\text{mm}^3$, while the mortar joints are 10 mm thick. The resulting eight of the prism is $H = 270$ mm. Note that mortar joints have smaller sizes than brick units; in fact, a recess of 7 mm is considered in the computations. The material mechanical parameters adopted here and derived from those reported in [9] are reported in Table 4. The brick tensile and compressive strengths are equal to 2.7 MPa and 22.6 MPa, respectively. In the experimental campaign, two series of specimens were tested, characterized by different composition of the mortar. Here, results obtained for series 2 are considered. As the proposed model discussed in the previous section accounts only for a perfect axial loading condition for the masonry prism, the effect of the load eccentricity investigated in [9] is not studied here.

Figure 19(a) illustrates the load-displacement curve in terms of the total base vertical reaction versus the applied displacement on the top of the masonry prism. The curve obtained by adopting the presented simplified model (continuous line) is compared with the corresponding experimental data (circle symbols). It can be noted that the numerical curve satisfactorily matches experimental outcomes. Figure 19(b) reports the evolution of the damages evaluated averaging the strain in the whole brick, computed in the centerline of the brick and in the mortar joints. As expected, damage grows more rapidly in the center of the brick as maximum tensile strain occurs in the middle of the brick.

		brick	mortar
E	[MPa]	2600	335
ν		0.05	0.20
σ_t	[MPa]	1.53	0.49
$\sigma_{t\ \max}$	[MPa]	2.7	0.74
α_t	$[\text{MPa}]^{-1}$	0.20	0.70
G_t	[MPa]	0.0125	0.0085
σ_c	[MPa]	20.00	7.40
$\sigma_{c\ \max}$	[MPa]	22.00	9.00
α_c	$[\text{MPa}]^{-1}$	0.50	1.00
G_c	[MPa]	0.58	1.05
η		1.00	1.00

Table 4: Axially loaded column: material parameters adopted for bricks and mortar.

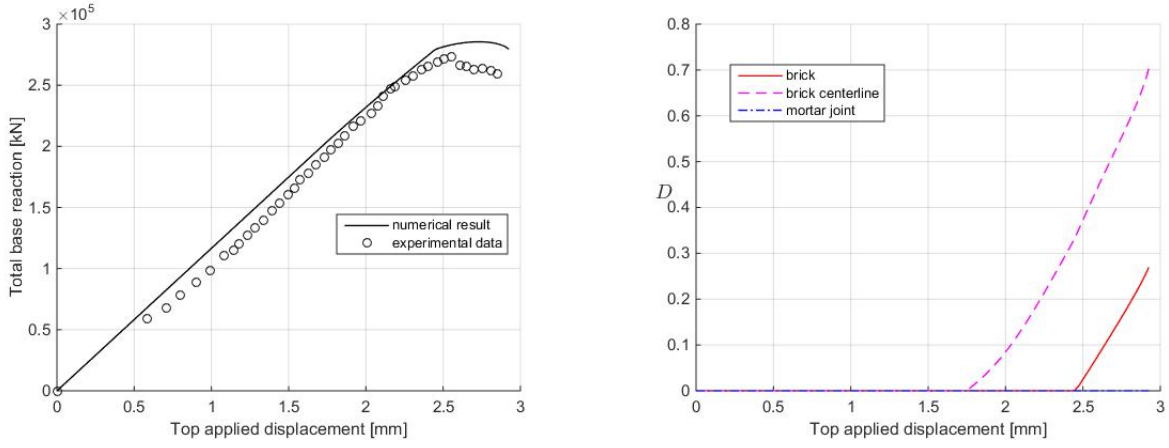

(a) (b)

Figure 19: Mechanical response of a masonry prism subjected to axial load; (a) total base reaction versus top applied displacement, (b) damage evolution in the brick, in the centerline of the brick and in the mortar.

6 Conclusions

A numerical procedure to investigate the nonlinear compressive response of masonry columns, separately modeling bricks and mortar, has been presented. To describe the masonry degrading mechanisms under compression loads, an isotropic damage model based on a simplified form of the Willam-Warnke criterion and an exponential evolution law has been adopted both for brick and mortar. Thanks to the adoption of some assumptions concerning the kinematic description of the 3D problem and the damage considered as constant in proper defined subsets of the analyzed masonry UCs, the governing equations are notably simplified. Moreover, the collocation technique has been used to solve the nonlinear problem of the UC subjected to axial compressive loads.

The proposed approach has been implemented in MATLAB and used to perform numerical tests on masonry prisms, characterized by different geometries and mechanical properties of the components (i.e. brick and mortar), giving reliable results in perfect agreement with those evaluated via a nonlocal 3D FE solution technique, introduced in FEAP. Moreover, the developed numerical applications have shown that the proposed numerical procedure is accurate, efficient and very fast in determining the overall response of the masonry prisms.

The numerical outcomes show that the increase of the brick compressive strength significantly increases the masonry overall compressive strength, although the latter is always lower than that of the bricks. Simultaneously, the reduction of the brick fracture energy makes the overall softening more severe. On the other hand, as expected, both the mortar compressive strength and fracture energy have an almost negligible influence on the masonry overall compressive response.

The developed model, properly modified, can be adopted to study the improvement in the mechanical response of a masonry column retrofitted by the FRP or FRCM jacketing systems. Moreover, it represents a valid tool to be extended to study the response of masonry columns subjected to combined axial and bending forces. Hence, the proposed kinematics has to be properly modified to account for the bending of the structural elements. Another interesting development is the extension of the proposed formulation to analyze the effects of the evolving damaging mechanisms on structural stability and buckling of the masonry column. Indeed, pioneer works have investigated these aspects for cracked column cross-section in presence of no- or low tensile strength material [17]. More recently, a 2D homogenized non-linear model was proposed including second order effects to analyze post-cracking and post-buckling behavior of slender URM walls [25].

Acknowledgement and Compliance with Ethical Standards

Funding:
This study was funded by ReLUIS (Italian Department of Civil Protection), MIUR-PRIN, University of Rome Sapienza CUP B86J16002300001.

Conflict of Interest:
The authors declare that they have no conflict of interest.

References

[1] D. Addessi. A 2D Cosserat finite element based on a damage-plastic model for brittle materials. *Computers & Structures*, 135:20–31, 2014.

[2] D. Addessi and E. Sacco. Enriched plane state formulation for nonlinear homogenization of in-plane masonry wall. *Meccanica*, 51(11):2891–2907, 2016.

[3] D. Addessi and E. Sacco. Nonlinear analysis of masonry panels using a kinematic enriched plane state formulation. *International Journal of Solids and Structures*, 90:194–214, 2016.

[4] M. Angelillo, A. Fortunato, A. Montanino, and M. Lippiello. Singular stress fields in masonry structures: Derand was right. *Meccanica*, 49(5):1243–1262, 2014.

[5] N. Augenti and F. Parisi. Constitutive models for tuff masonry under uniaxial compression. *Journal of Materials in Civil Engineering*, 22(11):1102–1111, 2010.

[6] A. Bacigalupo and L. Gambarotta. Second-order computational homogenization of heterogeneous materials with periodic microstructure. *ZAMM: Journal of Applied Mathematics and Mechanics*, 90(11):796–811, 2011.

[7] L. Berto, A. Saetta, R. Scotta, and R. Vitaliani. An orthotropic damage model for masonry structures. *International Journal for Numerical Methods in Engineering*, 55:127–157, 2002.

[8] D. Bigoni and A. Piccolroaz. Yield criteria for quasibrittle and frictional materials. *International Journal of Solids and Structures*, 41(11):2855 – 2878, 2004.

[9] A. Brencich and L. Gambarotta. Mechanical response of solid clay brickwork under eccentric loading. part i: Unreinforced masonry. *Materials and Structures*, 38:257–266, 2005.

[10] N. Cavalagli, F. Cluni, and V. Gusella. Evaluation of a statistically equivalent periodic unit cell for a quasi-periodic masonry. *International Journal of Solids and Structures*, 50(25-26):4226 – 4240, 2013.

[11] A. Cecchi and A. Tralli. A homogenized viscoelastic model for masonry structures. *International Journal of Solids and Structures*, 49:1485–1496, 2012.

[12] J.L. Chaboche. Continuum damage mechanics: Present state and future trends. *Nuclear Engineering and Design*, 105(1):19 – 33, 1987.

[13] N. Challamel, C. Lanos, and C. Casandjian. Strain-based anisotropic damage modelling and unilateral effects. *International Journal of Mechanical Sciences*, 47:459–473, 2005.

[14] C. Comi and U. Perego. Fracture energy based bi-dissipative damage model for concrete. *International Journal of Solids and Structures*, 38:6427–6454, 2001.

[15] M. Como. Virtual displacements principle, existence and uniqueness for elastic no tension bodies. *Meccanica*, 52(6):1397–1405, 2017.

[16] S. Fichant, C. La Borderie, and G. Pijaudier-Cabot. Isotropic and anisotropic descriptions of damage in concrete structures. *Mechanics of Cohesive-Frictional Materials*, 4:339–359, 1999.

[17] R. Frisch-Fay. Buckling of masonry pier under its own weight. *International Journal of Solids and Structures*, 16, 1980.

[18] K. S. Gumaste, K. S. Nanjunda Rao, B. V. Venkatarama Reddy, and K. S. Jagadish. Strength and elasticity of brick masonry prisms and wallettes under compression. *Materials and Structures*, 40:241–253, 2007.

[19] E. Gürses and C. Miehe. On evolving deformation microstructures in non-convex partially damaged solids. *Journal of the Mechanics and Physics of Solids*, 59(6):1268 – 1290, 2011.

[20] D. Halm and A. Dragon. A model of anisotropic damage by mesocrack growth; unilateral effect. *International Journal of Damage*, 5(4):384–402, 1996.

[21] H.K. Hilsdorf. Investigation into the failure of brick masonry loaded in axial compression. *Designing, Engineering and Constructing with Masonry Products, F.B. Johnson ed., Gulf Publishing, Houston, Texas*, pages 34–41., 1969.

[22] H.B. Kaushik, D.C. Rai, and S.K. Jain. Stress-strain characteristics of clay brick masonry under uniaxial compression. *Journal of Materials in Civil Engineering, ASCE*, 19(9):728–739, 2007.

[23] J. Mazars and G. Pijaudier-Cabot. Continuum damage theory-application to concrete. *Journal of Engineering Mechanics*, 115:345–365, 1989.

[24] C. Miehe and M. Lambrecht. A two-scale finite element relaxation analysis of shear bands in non-convex inelastic solids: small-strain theory for standard dissipative materials. *Computer Methods in Applied Mechanics and Engineering*, 192(5):473 – 508, 2003.

[25] G. Milani, M. Pizzolato, and A. Tralli. Simple numerical model with second order effects for out-of-plane loaded masonry walls. *Engineering Structures*, 48:98 – 120, 2013.

[26] S. Müller. Homogenization of nonconvex integral functionals and cellular elastic materials. *Arch. Rational Mech. Anal.*, 99(3):189–212, 1987.

[27] D.V. Oliveira. Mechanical characterization of stone and brick masonry. techreport 00-DEC/E-4, Department of Civil Engineering - University of Minho, 2000.

[28] E. Reccia, G. Milani, A. Cecchi, and A. Tralli. Full 3d homogenization approach to investigate the behavior of masonry arch bridges: The venice trans-lagoon railway bridge. *Construction and Building Materials*, 66(0):567–586, 2014.

[29] J.C. Simo and J.W. Ju. Strain- and stress-based continuum damage models-i. formulation. *International Journal of Solids and Structures*, 23, 1987.

[30] R. Sousa, J. Guedes, and H. Sousa. Characterization of the uniaxial compression behaviour of unreinforced masonry - sensitivity analysis based on a numerical and experimental approach. *Archives of Civil and Mechanical Engineering*, 15:532 – 547, 2015.

[31] R.L. Taylor. *FEAP-A finite element analysis program, Version 8.3*. Department of Civil and Environmental Engineering, University of California at Berkeley, California, 2011.

[32] C.V. Uday Vyas and B. V. Venkatarama Reddy. Prediction of solid block masonry prism compressive strength using fe model. *Materials and Structures*, 43:719–735, 2010.

[33] H. Welemane and C. Goidescu. Isotropic brittle damage and unilateral effect. *Comptes Rendus Mecanique*, 338:271–276, 2010.

[34] Willam, K. and Warnke, E.P. *Constitutive models for the triaxial behavior of concrete.* Proceedings of the International Assoc. for Bridge and Structural Engineering, vol. 19, 1975.